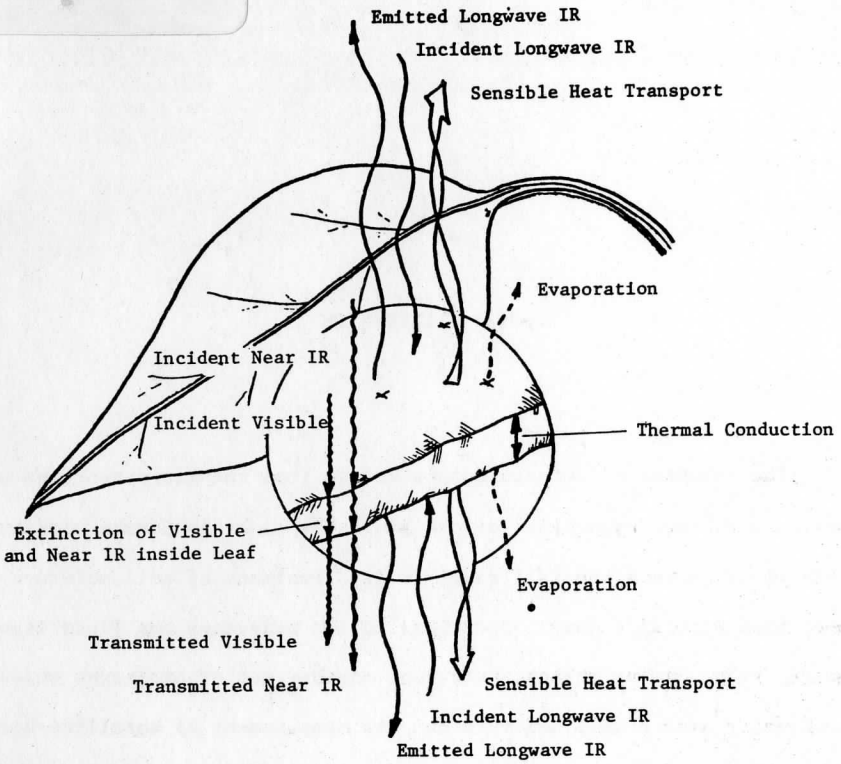

STUDIES OF SOUNDINGS AND IMAGING MEASUREMENTS

Final Scientific Report on NAS5-24136

1977

Space Science and Engineering Center
The University of Wisconsin-Madison
Madison, Wisconsin

June 1978

COVER ILLUSTRATION

The concerns of meteorologists extend from the microstructure of soils to the macroprocesses of the sun. The paper by George Diak in this report covers the full range in its treatment of soil moisture measurement from satellite data. Somewhere in the mid-range one finds leaves which, being living things, introduce another set of processes which profoundly affect soil moisture and its measurement by satellite-borne sensors. It is impossible to make the leaves disappear so that the satellite can see the ground unobscured, so Diak has included vegetation in his model in an attempt to see through it mathematically.

STUDIES OF SOUNDINGS

AND IMAGING MEASUREMENTS

STUDIES OF SOUNDINGS AND IMAGING MEASUREMENTS

Final Scientific Report on NAS5-24136

1977

The research in this document has been supported in whole or part by the National Aeronautics and Space Administration.

June 1978

Published for the Space Science and Engineering Center
by the
University of Wisconsin Press

Published 1978
The University of Wisconsin Press
Box 1379, Madison, Wisconsin 53701

The University of Wisconsin Press, Ltd.
70 Great Russell Street, London

First Printing
Printed in the United States of America
ISBN 0-299-97059-0

This work is a result of research sponsored by NASA, the National Aeronautics and Space Administration, under Contract Number NAS5-24136. The U.S. Government is authorized to produce and distribute reprints for governmental purposes notwithstanding any copyright notation that may appear hereon.

Correspondence concerning editorial matters should be addressed to:

Space Science and Engineering Center
University of Wisconsin
1225 West Dayton Street
Madison, Wisconsin 53706

Orders for copies of this report should be addressed to:

The University of Wisconsin Press

PRINCIPAL INVESTIGATOR: VERNER E. SUOMI

CONTRIBUTORS: W.R. BRYSON
G. DIAK
R. GIRD
M. PECKNICK

UNIVERSITY OF WISCONSIN

CONTENTS

Technical Articles Page

PREFACE

Last year we published what we thought was the last report in this lengthy series which NASA has supported since 1967. However, some studies needed to be continued a little longer to be sure the work, and the people involved, did not become side-tracked. With the concurrence and financial support of our NASA friends, four young scientists have had the opportunity to advance their studies and to prepare this report. I am pleased by their work, I am proud of them, and I am grateful to NASA for the additional support.

Verner E. Suomi
Principal Investigator

SNOW EXTENT MEASUREMENTS FROM GEOSTATIONARY SATELLITES USING AN INTERACTIVE COMPUTER SYSTEM

Ron Gird

ABSTRACT

This paper describes the use of an interactive computerized data access system (McIDAS) to evaluate the extent of snow fields in the Salt and the Verde River Basins in central Arizona from satellite images. This study was based on real-time visible image data of 1 km resolution generated by the eastern GOES (Geostationary Operational Environmental Satellite) in orbit about 20,000 nautical miles above the earth at 0^{o}N latitude, 75^{o}W longitude.

Because GOES produces an image about every half hour, one "best" image of optimum clarity could be selected for each study day. These images were then processed and aligned by the McIDAS system for sequential chronological study.

This new method for preparing Snow Extent Measurements (SEM) is compared to the current operational SEM techniques used by the National Environmental Satellite Service (NESS). It is suggested that the use of real-time satellite data, the ability to select "optimum" images for study, and the automated analysis methods made possible by the GOES/McIDAS technique could improve the operational SEM program now in use at NESS. Modifications to the GOES/McIDAS technique and other possible applications of the system are also suggested.

1. INTRODUCTION

Although world population is increasing, the world's water supply remains constant because within the hydrological cycle, water is neither created nor destroyed. For this reason, efficient and intelligent management of water supplies is essential. The snow cover in mountain regions and in river basins constitutes an important segment of the water supply; many cities and large regions of the country depend partly upon snow cover for their water supply. The city of Phoenix, Arizona is one example of a large U. S. city whose water supply is linked to distant snow cover.

Water management first requires an accurate knowledge of the location, amount, and melting rate of snow-held water. Snow cover measurements can provide valuable information about potential water supply, as well as such related topics as irrigation potential, water run-off, and flood control.

Weather satellite data provides much of the needed information concerning snow cover. Accurate snow interpretation and mapping from weather satellites has been demonstrated by Barnes and Bowley (1966, 1974); in 1972, the National Environmental Satellite Service (NESS) established an operational

snow cover program (Schneider et al., 1976). Satellite-derived Snow Extent Measurements (SEM) for specific river basins within the United States have been provided since then by NESS to selected National Weather Service Forecast Centers for use in various hydrological models.

Current SEM operational programs rely heavily on data from polar-orbiting satellites and on manual analysis of this data. This approach presents several inherent drawbacks. For example, real-time polar orbiting satellite data is not readily available. In addition, only one daytime image is generated for a specific earth location — an image with a very low solar zenith angle (0930 local). This low solar angle means that shadows obscure parts of the snow field. Additionally, the daily image may be obscured by cloud cover.

Manual analysis of satellite data to produce a SEM involves many complex coordinate transformations; this manual process takes time and introduces the chance of error. Furthermore, only one analyst at a time can view an image and make a measurement; discussions of image interpretation and measurements between colleagues is difficult.

A computer-based interactive system would eliminate the present drawbacks and would permit the use of new techniques such as elevation slicing and hourly snow-melting rate calculations to upgrade the current NESS SEM program. The purpose of this study was to examine one computer system which could incorporate these new concepts.

First, it will be shown that this new system can produce results at least comparable to the current NESS operational SEM program. Second, new concepts for SEM, unique to this new system, will be described.

This study used real-time data from the Geostationary Operational Environmental Satellite (GOES), analyzed by an interactive computer system to calculate SEM. Full resolution (1 km) visible data from the eastern GOES satellite (0°N, 75°W) was selected for this study; the GOES visible sensor detects radiation between 0.55-0.75μm. A complete description of the GOES system is given by Bristor (1976). The University of Wisconsin's Man-computer Interactive Data Access System (McIDAS) used to make the SEM calculations is described by Smith (1975), and by Chatters and Suomi (1975).

The GOES and McIDAS combination provided many opportunities to improve and increase the flexibility of SEM. The GOES satellite provides real-time data and generates more than one image per day, so it was possible to select an optimum image for each specific basin, taking into account such factors as solar zenith angle and cloud cover. A recent study by Breaker and McMillan (1975) indicated that daily and perhaps hourly snow-melting rates could be obtained from GOES image film loops. In a related report, Schumann (1975) and Warskow et al. (1975) indicated the need for such hourly snow-melting rates during periods of high run-off and minimum reservoir storage capacity -- rate calculations that are extremely important for desert cities like Phoenix, Arizona.

Throughout this report, reference will be made to a Registered Image Sequence (RIS). This is a series of GOES full-resolution visible images viewed on the McIDAS video component in chronological order and navigated to within ±1 satellite pixel. For a complete description of the McIDAS navigation system, see Phillips and Smith (1975). During a RIS, the land masses remain fixed, clouds may move, form and dissipate, while snow fields change shape and character in response to meteorological conditions. By studying a RIS that is compiled from real-time data, the McIDAS analyst can compute real-time hourly snow-melting rates. The McIDAS software can also eliminate clouds from a RIS to create a SEM from a composite image. The usefulness of cloud-free composite images for SEM has been established by McClain and Baker (1969), although they did not use real-time data. The cloud elimination technique used in this study is described in a later section.

Finally, it should be noted that all SEM calculations are performed by the McIDAS computer; this reduces errors by reducing the number of transforms in the SEM calculation process.

2. EXPERIMENTAL PROCEDURE

The basins selected for this study were the Salt and Verde river basins located in central Arizona. Figure 1 shows the basins as viewed from the eastern GOES satellite position. These basins were selected for many reasons. They are routinely mapped by the NESS SEM program, so comparison of NESS vs. GOES/McIDAS results would be straightforward. Second, these basins have many visible landmarks (Lake Roosevelt, Mormon Lake, and the Little Colorado River) which would be helpful in establishing the accuracy of the McIDAS navigation. (Navigation is required for any type of RIS analysis or transformations). Third, five National Weather Service stations are located in or around the basins (Figure 1), so conventional data (including weather radar reports) could be used to examine closely the winter history of the basins. Finally, the basins are frequently cloud-free even during the winter months, thereby making it possible to compile a long-term data set for snow extent analysis.

This study was conducted in three phases: the initialization phase, the data collection phase, and the analysis phase. In the initialization phase, the basin perimeters were defined in terms of latitude and longitude points and stored inside McIDAS. Second, a preliminary GOES image data set was collected in which both basins were free of both cloud cover and snow. Later, in the data collection phase, GOES image data was saved for those days on which an SEM looked feasible. In the final analysis phase, SEM's were performed using McIDAS.

Initialization Phase

As the first step in defining the basin perimeters, an accurate map of the basin areas with the perimeters outlined was obtained from the United States Geological Survey in Phoenix, Arizona. The map was a Phoenix Sectional Aeronautical Chart, scale 1:500,000. A number of latitude and longitude

points were selected from the perimeter outlines--56 and 89 points for the Salt and Verde basins, respectively. These grid points were then punched onto computer cards and read into McIDAS. Once stored in McIDAS, the perimeter outlines could be displayed on the McIDAS video at any time by typing in a single line of command via the keyboard. A denser network of points could have been used, but for this project, it was not deemed necessary.

The second part of the initialization phase was the collection of the preliminary data set. These images were used to familiarize the McIDAS operators with the basin geography (landmark features). Numerous landmarks were clearly visible within the area of interest; the most prominent are Lake Roosevelt, Mormon Lake, Mount Baldy, and the Little Colorado River. The preliminary data set was collected from December 7, 1976 to December 24, 1976; a local noon image, 1900 GMT, was selected as the primary data collection time for the entire study. During this 17-day period, nine images were collected but only three images satisfied the above requirements and were of acceptable quality (i.e., had no data drop-outs). The three images were then navigated via McIDAS and assembled to form the initial RIS--the start of the "winter history" for both basins.

In the final part of the initialization phase, the accuracy of the computer-generated basin perimeters was checked. First, the basin perimeters and GOES satellite data were viewed simultaneously on the McIDAS-CRT. This image was compared to the aeronautical chart and errors in the selected perimeter points were corrected. Second, the total area of the two basins was computed using the GOES data and McIDAS. The basin perimeters were traced using the McIDAS video cursor, controlled by a manual joy-stick; the McIDAS software then derived the outline. The area results, expressed in terms of number of satellite pixels, in km^2, and in nm^2, differed by less than 2% (33,235 km^2 vs 32,686 km^2) from the ground truth calculations of Suchman (1975).

Data Collection Phase

The data collection phase of the project took place between January 4, 1977, and February 1. 1977. During this phase, all possible 1900 GMT cloud-free GOES images of the basins were collected using McIDAS. Daily checks of the synoptic weather conditions were conducted at 1400 GMT and updated at 1800 GMT, using the National Weather Service products collected by the UW - Madison, Department of Meteorology. If all conditions at 1800 GMT looked favorable, McIDAS ingested the 1900 GMT GOES visible data centered on Phoenix, Arizona. After ingest, the data was archived onto magnetic tape so that the SEM analysis could be carried out at any later time (depending on McIDAS availability). During this 28-day period a total of 14 images were collected and saved. Only five of the 14 images were completely cloud-free and were used for SEM; the remaining nine had some degree of cloudiness, mostly thin cirrus, in the basins.

SEM Phase

Prior to final SEM analysis, the image to be studied was incorporated into the already existing RIS in the following way: The first three images of the RIS were the three snow-free, cloud-free images from the preliminary data set. The fourth image of the RIS was the first image of the data collection phase, the fifth image would be the second image of the data collection phase, and so on, until all five images from the data collection phase were incorporated into the RIS. It was quite easy to detect minor changes in the snow fields between two sequential images; this "historical" RIS was a valuable aid in maintaining a consistent SEM product throughout the project. (A further discussion is presented in the Results section).

Once the specific image was incorporated chronologically into the RIS and compared to previous images and the trend of the snow field changes was established, the SEM analysis was conducted.

To make an accurate SEM, each GOES image had to be displayed as a four-fold expansion on the McIDAS video (16 video pixels for every satellite pixel). Because of this expansion, analysis of each basin had to be carried out in four sub-sectors. A second expanded image --"yesterday's" image relative to the five images of the data collection set -- was displayed alternately on the McIDAS video to help detect very small changes in the snow fields. While these images alternated on the video, the cursor was used to outline the snow fields. Once a snow field within the sub-sector was outlined, a second tracing (using the cursor) was completed. Completion of this second tracing automatically invoked the area calculation software of McIDAS, and the area calculation for the snow field within the sub-sector was displayed and printed out. This snow-field area calculation was expressed in terms of the number of satellite pixels and in km^2. Once the areas for all the snow fields were calculated for the sub-sector, another sub-sector was selected and appropriate steps repeated. After the analysis of all sub-sectors was completed, the snow field calculations for each basin were added together. Since the total area of the two basins was calculated from the preliminary data set, an SEM could be calculated for the two basins.

3. CLOUD SUBTRACTION TECHNIQUE FOR SEM

A powerful feature of the McIDAS software is the Cloud Subtraction Routine (CSR). For a complete description of the Cloud Subtraction Routine see Mosher (1977). In order to produce meaningful results, the CSR must be performed on an RIS. Inside McIDAS, the CSR matches up to six images from the RIS, scanning the images and retaining only the darkest pixels at each location from the RIS images. The resulting composite image is thus composed of the darkest pixels from the RIS, in effect eliminating the lighter clouds moving over the darker land.

To demonstrate the usefulness of the CSR in doing SEM calculations, a RIS was compiled from 1830, 1900 and 1930 GMT images for February 6, 1977. In each of the three images, both basins were obscured by clouds and no SEM could have

been prepared from any of the individual images. The CSR successfully eliminated the clouds from the three images and produced a composite image suitable for a SEM. The results of this technique will be discussed in the following section.

4. EVALUATION OF RESULTS

Comparison of Methods

The GOES/McIDAS SEM results show good agreement when compared with the NESS products (Figure 2) during the first part of this study (January 10-15, 1977). The second part of this study (January 16-28, 1977) shows the GOES/McIDAS products to be approximately three to five percent less than the NESS polar-orbiting-based products. A similar result has been previously observed by Schneider and McGinnis (1977). Another significant difference was noted. From January 13 to January 15, 1977, the NESS products showed an increase in the snow cover for the Verde Basin, while the GOES/McIDAS product implied no change in the snow cover for approximately the same period. Additionally, a check of National Weather Service Radar Reports during this period indicated no precipitation had occurred within the Verde Basin. Therefore, the increase in snow cover reported in the NESS analysis appears to be an error -- the type of error that might be expected using the current manual techniques during periods of little or no change in the snow cover. The use of an RIS could help eliminate this type of error, since small or zero changes in the snow cover between any two days are easily detected when viewing the images within a RIS. The RIS thereby provides continuity for sequential SEM operations.

A comparison of SEM results for January 10, 1977 is shown in Figure 3, indicating an apparent loss of detail in the snow cover outlines produced by GOES/McIDAS. This difference, however, is not real. It results from the transfer of the SEM analysis from the McIDAS CRT to the worksheet; the actual outlines generated by McIDAS and used for the SEM did contain more detail. The two products show good agreement with the minor exception of the snow-capped mountain peaks located in the southern part of the Verde basin. Old or new snow on mountain peaks showed up very clearly when the analysis image was compared to a snow-free image in the RIS.

Satellite Pixel vs Km^2 Results

A comparison of GOES/McIDAS-generated SEM results using both satellite pixels and km^2 areas was conducted. The results, shown in Table 1, indicate only second-order differences between the two methods. The shape of the satellite pixel is approximately square for this basin location, although the pixel distortion does get worse the further away an earth pixel is located from the GOES satellite subpoint (0°N, 75°W). The navigation software in McIDAS calculated the approximate pixel dimensions in the area of the basins as 0.59 nm wide and 0.68 nm long. Although the units of area used to calculate SEM (satellite pixel or km^2) do not matter for these two basins, other basins analyzed by GOES/McIDAS would have to be treated as individual cases when selecting the area units.

Cloud Subtraction Results

The SEM results generated by McIDAS from the cloud-free composite image agreed favorably with the NESS product. The GOES/McIDAS SEM for the Salt basin for February 6, 1977 indicated 11% snow cover; the NESS product for February 7, 1977 showed the Salt basin to be 17% snow covered. The clouds that were eliminated from the images were estimated to be of either the mid-level or high-level type, and they did produce significant shadows on the ground which were not eliminated from the composite image. Further investigation of the cloud elimination scheme is recommended.

Analysis Time

The time required to complete an SEM with the GOES/McIDAS system averaged 30 minutes per image throughout this study, but this time can fluctuate ± 15 minutes depending upon the complexity of the snow cover. New snow cover, which covers a larger, more uniform area, is easier to analyze than older, patchy snow cover. The GOES/McIDAS analysis time is approximately equal to the current manual NESS operation. The significant difference between methods is that a GOES/McIDAS analysis can be completed within an hour after image reception time, whereas the current manual NESS operation takes 24 hours or more to complete. It should be noted, however, that an improvement in analysis time was not an objective of this study.

Errors

The most significant source of error in the GOES/McIDAS scheme is the experience of the analyst in snow-mapping, although experience and confidence increased rapidly (and errors declined) during this study. A second source of error was in the McIDAS tracing software routines. The software requires the storage of satellite pixels in order to define the snow cover outline. Because this storage array is limited, the McIDAS analyst had to rapidly trace the outlines in order to avoid overflowing the storage array. Faster tracing implies fewer satellite pixels to be stored. This limitation would be a serious problem when performing an SEM that required fine detail in the outlined basin. Since these tracing software routines are still considered developmental, corrections could be applied to the operational version. Another source of error (related to the tracing problem) was the extreme sensitivity to trace details as small as one or two pixels (isolated snow-capped mountain peaks); considerable practice was required.

5. CONCLUSIONS AND RECOMMENDATIONS

This study indicates that the GOES/McIDAS SEM process can produce reliable, consistent snow-mapping results. Further, interactive computer systems like McIDAS appear to offer many advantages over the present manual techniques. Improvements, however, can be made in the McIDAS software. Additional software could be included to introduce semi-automatic tracing techniques; parts of the snow cover that extend up to the basin perimeters could be outlined automatically since the basin perimeter is defined within the computer in terms of latitude and longitude. Total automation of SEM seems remote, however; accurate definition of snow cover still requires human interpretation.

On the basis of this study, it is recommended that snow extent mapping using the GOES/McIDAS method should be incorporated into the present snow-mapping program of the National Environmental Satellite Service. Further investigations should examine the following topics: selection of a wider variety of snow basins for study; use of polar-orbiting satellite data with McIDAS for the mapping of northern basins; and the use of techniques such as elevation slicing and cloud elimination schemes to further improve SEM study.

ACKNOWLEDGEMENTS

Special thanks to my advisor, Dr. Verner Suomi (Space Science and Engineering Center), for his direction and continual support. Thanks also to Tom Haig (Space Science and Engineering Center), Stan Schneider (National Environmental Satellite Service), and Herb Schumann (United States Geological Survey) for their excellent cooperation and information. Technical assistance and support was graciously provided by J. T. Young and Dee Cavallo (Space Science and Engineering Center), and by Gene Legg (National Environmental Satellite Service).

This work was supported under NASA contract NAS5-21798.

REFERENCES

Barnes, J.C., and C.J. Bowley, 1966: Snow Cover Distribution as Mapped from Satellite Photography. Final Report, Contract No. Cwb-11269, Allied Research Associates, Inc., Concord, MA, 108pp.

Barnes, J.C., and C.J. Bowley, 1974: Handbook of Techniques for Satellite Snow Mapping, ERT Document No. 0407-A Environmental Research and Technology, Inc., Concord, MA, 95pp.

Breaker, B.C., and M.C. McMillan, 1975: Sierra Nevada Snow Melt from SMS-2, Operational Applications of Satellite Snowcover Observations, South Lake Tahoe, CA, pp. 187-198.

Bristor, C.L., 1975: Central Processing and Analysis of Geostationary Satellite Data, NOAA Technical Memorandum NESS 64, U.S. Department of Commerce, Washington, DC, 155pp.

Chatters, G.C., and V.E. Suomi, 1975: The Applications of McIDAS, IEEE Transactions on Geoscience Electronics, GE-13, pp. 137-146.

McClain, E.P., and D.R. Baker, 1969, Experimental Large-Scale Snow and Ice Mapping with Composite Minimum Brightness Charts, ESSA Technical Memorandum NESCTM 12, U.S. Department of Commerce, Washington, DC, 19pp.

Mosher, F.R., 1977: Composite Images Using Navigated SMS/GOES Data, Studies of Soundings and Image Measurements, Final Report on NAS5-21798, Space Science and Engineering Center, University of Wisconsin-Madison, Madison, Wisconsin, pp. 111-126.

Phillips, D., and E. Smith, 1973: Geosynchronous Satellite Navigation Model, Studies of the Atmosphere Using Aerospace Probes, NOAA Grant NG-26-72, Space Science and Engineering Center, University of Wisconsin, Madison,WI, pp. 253-271.

Schneider, S.R. and D.F. McGinnis, Jr., 1977: Spectral Differences between VHRR and VISSR Data and their Impact on Environmental Studies, Proceedings of the American Society of Photogrammetry, Washington, D.C., pp. 470-480.

Schneider, S.R., D.R. Wiesnet and M.C. McMillan, 1976: River Basin Snow Mapping at the National Environmental Satellite Service, NOAA Technical Memorandum NESS 83, U.S. Department of Commerce, Washington, DC, 19pp.

Schumann, H.H., 1975: Operational Application of Satellite Snowcover Observations and LANDSAT Data Collection Systems Operations in Central Arizona, Operational Applications of Satellite Snowcover Observations, South Lake Tahoe, CA, pp. 13-28.

Smith, E.A., 1975: The McIDAS System, IEEE Transactions on Geoscience Electronics, GE-13, pp. 123-136.

Warskow, W.L., T.T. Wilson Jr., and K. Kirdar, 1975: The Application of Hydrometeorological Data Obtained by Remote Sensing Techniques for Multi-purpose Reservoir Operations, Operational Applications of Satellite Snowcover Observations, South Lake Tahoe, CA, pp. 29-37.

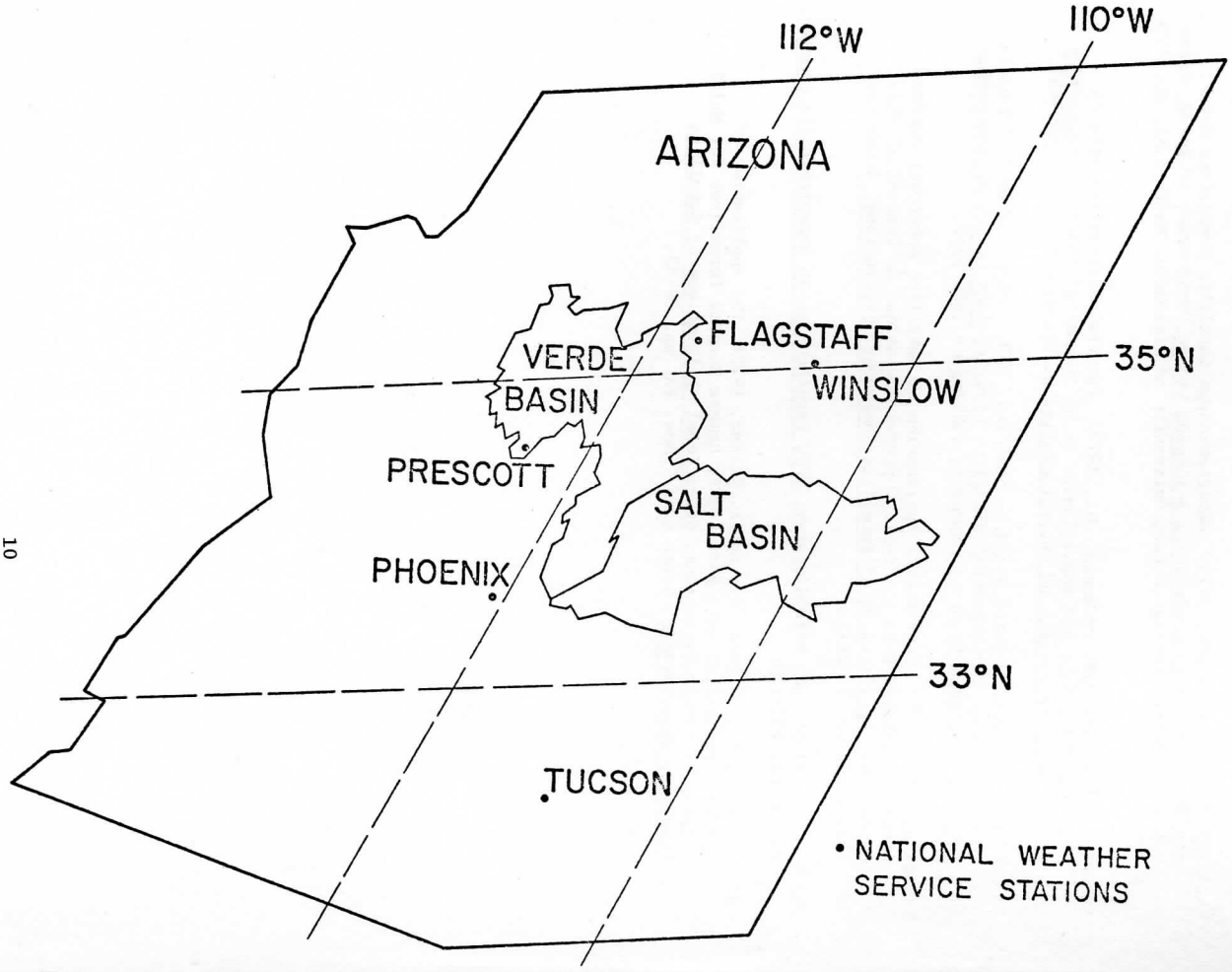

FIGURE 1: Salt and Verde River Basins, viewed from eastern GOES satellite position.

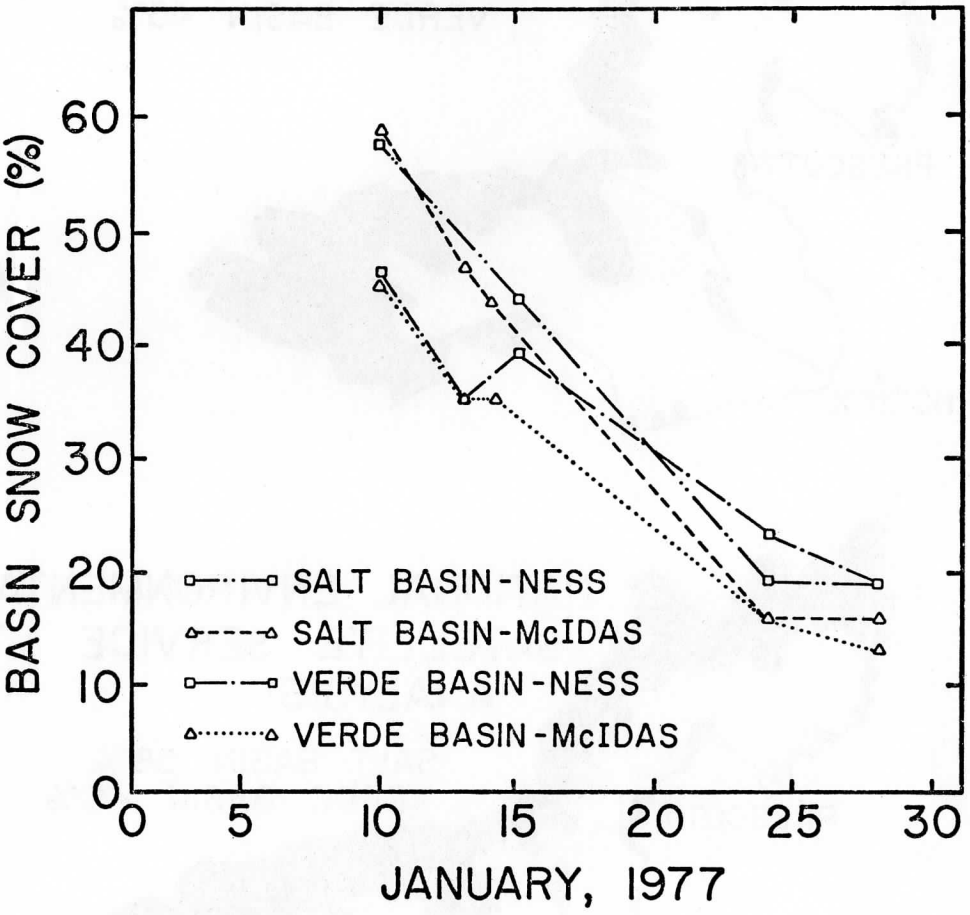

FIGURE 2: Comparison of Snow Extent Measurements (SEM) for the Salt and Verde River Basins.

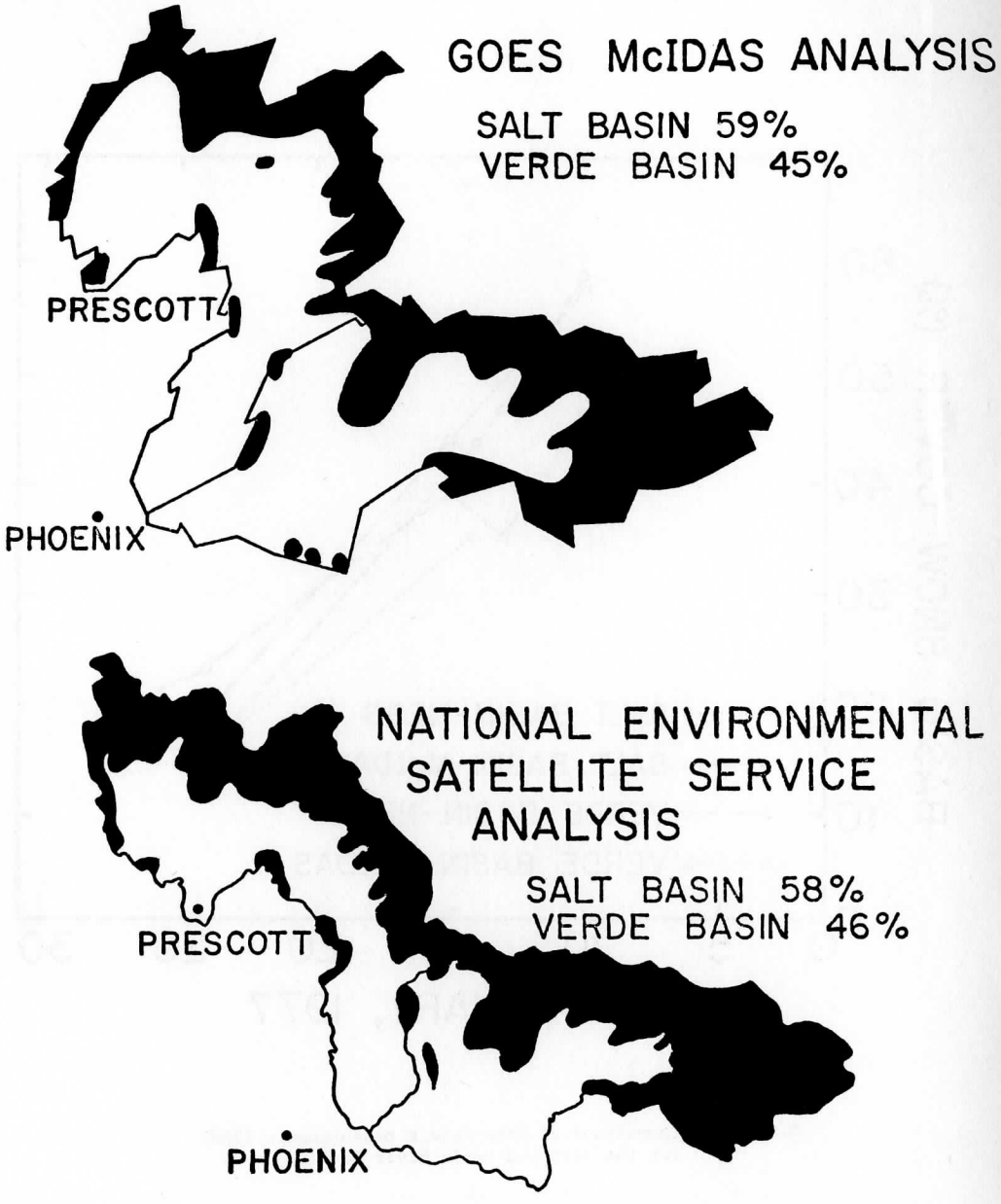

FIGURE 3: Comparison of SEM results for GOES/McIDAS and NESS analyses for 10 January 1977. Black areas indicate snow cover.

TABLE 1

Comparison of Snow Extent Measurements (SEM) using pixel and square-kilometer results.

	SALT BASIN		VERDE BASIN	
Date	%-Pixels	%-km^2	%-Pixels	%-km^2
1-10-77	0.5936	0.5931	0.4431	0.4457
1-13-77	0.4705	0.4647	0.3470	0.3458
1-14-77	0.4369	0.4320	0.3476	0.3455
1-24-77	0.1515	0.1520	0.1571	0.1538
1-28-77	0.1294	0.1270	0.1098	0.1076

UTILIZATION OF SATELLITE AND SURFACE OBSERVATIONS IN A GRAVITY WAVE STUDY

Michael J. Pecnick

ABSTRACT

An analysis of a gravity wave incident is presented, using both surface and satellite observations. The gravity wave was isolated at the surface using a pressure perturbation analysis. The gravity wave had a propagation speed of about 30 m s^{-1}, a horizontal wavelength of about 200 km, and an amplitude as large as 8.47 mb. Surface wind divergence fields agreed with these findings.

Satellite observations were used to find the magnitude and speed of the wave at upper levels through infrared image analysis. Wind fields, obtained by the cloud tracking method, were used to derive divergence patterns; these patterns were then used to check the dynamic consistency of the infrared analysis results. These findings were then coupled with the surface information to obtain a vertical structure of the wave. This, in turn, led to an improved estimate of the location of the energy source of the wave.

1. Introduction

Surface weather patterns are often affected by travelling pressure disturbances, many of which are accompanied by fluctuations in the wind field. Young and Richards (1974) found that late March is the most likely time of occurrence for these disturbances in the Midwest and Great Lakes region of the United States. These disturbances possess the characteristics of subsynoptic internal gravity waves, with phase speeds ranging between 10 to 40 m s^{-1}, wavelengths between 100 to 400 km, and periods ranging from 30 minutes to 4 hours (Brunk, 1949; Ferguson, 1967; Eom, 1975; Uccellini, 1975). Internal gravity waves propagating through an undisturbed atmosphere have a shortest period given by the Brunt-Vaisalla period, typically about 10 minutes.

Several articles concerning the properties of atmospheric gravity waves have either stated the need for investigating their vertical structure (Uccellini, 1975), or have used numerical or analytical models to simulate possible characteristics of these waves at levels above the surface (Goldie, 1925; Wiin-Nielsen, 1965; Eom, 1975). The purpose of this paper is to present evidence that gravity wave features at upper levels in the troposphere can be identified using satellite imagery, and that by coupling this information with surface data, some features of the vertical structure of gravity waves can be inferred.

The gravity wave incident of 27 March 1975 is investigated. The surface wave is described by a pressure perturbation analysis constructed from barograph traces. Further surface wave verification is found by a surface divergence analysis. In addition, imagery from Synchronous Meteorological Satellite-I (SMS-I) is used to acquire information concerning the gravity wave in the upper troposphere. An infrared imagery analysis is presented to determine the magnitude of the wave and improve estimates of its phase speed. A divergence analysis, using cloud motion winds, is used to check the dynamic consistency of the observations. These results are then combined to ascertain the vertical structure of the gravity wave.

2. Synoptic Situation and Surface Wave Analysis

On 27 March 1975, a deep cyclone was centered in western Kansas. An occluded front extended from Kansas and Nebraska into Oklahoma, and a strong cold front stretched southward through Oklahoma and Texas (Figure 1). This system moved slowly northward during the day. At upper levels a cut-off low, associated with the surface cyclone, prevailed to 300 mb (Figure 2). A jet stream stretching from the Texas panhandle to eastern Nebraska propagated toward the north-northeast and had maximum wind speeds of 60 m s^{-1} near the 300 mb level near Topeka, Kansas. In addition, a lower level jet stream was observed in eastern Oklahoma during the earlier portions of the day, with winds exceeding 35 m s^{-1} near the 850 mb level.

Upper air soundings throughout the Midwest, at both 1200 GMT 27 March and 0000 GMT 28 March, indicated stable frontal layers in the lower troposphere. Above these stable layers, and most prominent on the 0000 GMT 28 March soundings, the atmosphere exhibited conditionally unstable layers; portions of the Peoria, Illinois and St. Cloud, Minnesota soundings revealed superadiabatic layers near the 300 mb level (Figure 3). There were some areas of strong vertical wind shear observed, with an especially strong directional wind shear near the 300 mb level at St. Cloud.

It was in this synoptic environment that a strong pressure perturbation was observed moving eastward across the Midwest from 1600 GMT 27 March to 0400 GMT 28 March. Upon inspection of barograph traces, the perturbation was traced back into Nebraska and Kansas as early as 1200 GMT 27 March. Stations throughout Minnesota, Iowa, Illinois, and Wisconsin reported the greatest pressure falls, accompanied at some stations by strong wind gusts. There was no convection associated with the pressure perturbation. At Rochester, Minnesota, the pressure fell 4.40 mb in fifteen minutes (Figure 4), while winds increased from 30 kts to 38 kts with gusts up to 64 kts. It should be noted that the maximum wind was observed when the surface pressure reached its minimum. At LaCrosse, Wisconsin, the surface pressure dropped 7.45 mb in twenty minutes, although wind gusts were not as strong as those at Rochester. This may be because the LaCrosse reporting station is located in a north-south river valley which may moderate any easterly wind increases.

The period of this traveling perturbation was of the order of 2 to 3 hours, and the propagation speed was about 30 m s^{-1}. This pressure perturbation was not readily discernible with a conventional pressure analysis. Therefore, to improve estimates of the location, wavelength, amplitude, and trace speed of the perturbation, a pressure perturbation analysis was done on 35 of the 140 barograph traces available from National Weather Service stations in the Midwest. Included in the 35 stations were all stations in Iowa, Minnesota, Wisconsin, and Illinois, and some stations in Missouri. Because of the large amplitude of the perturbation, it was necessary only to eliminate the synoptic trend of falling pressure from the barograph traces caused by the approaching cyclone. This was done by fitting the barograph trace at each location with a linear least-squares approximation. The time for which the approximation was fitted was between 1800 GMT 27 March and 0600 GMT 28 March (Figure 5). The perturbation pressures at each location were found by subtracting the linear trend pressure trace from the actual pressure trace.

The results of the perturbation analysis were quite successful (Figure 6). The analysis did isolate the pressure perturbation from the synoptic environment; the pressure perturbation appeared as an extended, organized, negative perturbation area in the analysis. It should be noted that due to the sparse station density, spatial aliasing of the perturbation analysis was a potential problem. For this reason, the perturbation analyses were plotted for every 15 minutes, then cross-checked with the continuous barograph traces to maintain space-time continuity, especially when the negative perturbation area was between stations.

As shown in Figure 6, the pressure perturbation (resembling a portion of a plane wave) was already developed over central Iowa by 2030 GMT. The perturbation moved east-northeast across Iowa and Minnesota into Wisconsin and Illinois with a propagation speed of 32 m s^{-1} relative to the surface. The wavelength of the perturbation, which is twice the width of the negative perturbation area, was approximately 200 km. The amplitude of the perturbation remained fairly constant at 5.1 mb (0.15 in. Hg.), although it intensified to over 8.5 mb (0.25 in. Hg.) in the vicinity of the Minnesota-Wisconsin border near 2200 GMT.

With a propagation speed of 32 m s^{-1}, and a wavelength of the order of 200 km, the possibility that the pressure perturbation was the surface pressure response to gravity wave motions was quite evident. The stability of the atmosphere--with stable layers near the surface and saturated, conditionally unstable layers above--was conducive to the trapping of the energy of internal gravity waves (Lindzen and Tung, 1976), allowing for the longer duration of a wave at the surface.

In Figure 7, surface wind divergence patterns for 2300 GMT 27 March and 0000 GMT 28 March are shown. These patterns were derived from winds obtained by hourly observations at National Weather Service stations. In both cases, divergent motions were located east of the axis of the pressure perturbation

trough; these patterns of divergence moved with the wave, as they did for previous periods. This is consistent with the theory for a gravity wave propagating toward the east, which postulates that in a propagating, subsynoptic gravity wave, there must be divergence ahead of the wave trough region. (See Appendix A for a brief description of the gravity wave theory used.) These conditions are also present in the gravity wave analyses presented by Eom (1975) and Uccellini (1975).

Because of the consistency between the features of the 27 March incident and theoretical gravity wave features, along with the similarities between this case and the cases just mentioned, this moving perturbation was determined to be the surface pressure response to gravity wave motions.

3. Upper Level Analysis

SMS-I images were used to acquire information concerning the gravity wave at levels above the surface. During the period in which the gravity wave was observed at the surface, the Midwest was overcast by thick clouds, topped with a cirrus shield. The altitude of this cirrus shield was between 300 and 400 mb, determined using the Mosher method of determining cloud height (Suomi, 1975); this method also is briefly discussed by Suchman and Martin (1976). From 2200 GMT to 2330 GMT, a northwest-to-southeast-oriented depression appeared in the cirrus shield top. The images during this period were analyzed to investigate the possibility that this depression was a feature of the gravity wave at the surface.

There are several reasons for the analysis being confined to this period. The depression did not appear before 2200 GMT, eliminating the possibility of analysis of any previous images. After the 2330 GMT image was received, local sundown occurred, making visible imagery useless, while navigational problems prevented the use of later infrared images. It should be emphasized that during the period in which the cloud depression was most evident, the gravity wave was most intense at the surface.

Since the pressure trace of the surface gravity wave was of the form exhibited in Figure 4 (i.e. a rapid fall in pressure followed by a rapid rise), gravity wave theory (see Appendix A) dictates that such a gravity wave would appear at higher levels as a depression in the cloud deck. The maximum downward parcel displacement due to gravity wave motions occurs ahead of the minimum pressure, which is reached in the wave trough. From above, the depression would then take the form of a warm area, relative to the surrounding cirrus shield, since the air parcels would be warmed by pseudo-adiabatic and then dry adiabatic compression as the gravity wave motions caused downward displacement.

To find the magnitude of this displacement, and to provide a better estimate of its speed and location, digital infrared brightness values were analyzed. In this process, the digital brightness values of full resolution

infrared images (picture element size: 2 nautical miles) were output. Since each digital brightness value corresponded to a certain cloud-top temperature, the depression appeared as a relatively dark area on each infrared image. Much care was taken to eliminate possible effects of differential heating on one side of the depression by the sun, which was on the horizon; the analysis was cross-checked with the visible images for each time to confirm that warm areas were not due to local solar heating.

The outlines of the cloud depression from 2200 GMT to 2330 GMT obtained from the infrared analysis are presented in Figure 8. Because the cloud depression became better developed in the latter two periods, most conclusions were made concerning the actions of the depression at these times. The difference in temperature from the edge of the depression to its warmest point tends to be about 8°C. Relating this information to sounding data obtained at 0000 GMT 28 March, a temperature difference of 8°C would correspond to a difference in altitude of about 35 mb, or 770 m. This pressure difference was the distance that a parcel would travel by pseudo-adiabatic and dry adiabatic processes as the cloud depression passed. This distance would be analogous to the isentropic displacement amplitude of the gravity wave (assuming the cloud depression was due to gravity wave activity).

The depression moved at a speed of approximately 33 m s^{-1}, relative to the ground, almost perpendicular to the surface flow. The cloud depression propagated at a speed of over 30 m s^{-1} relative to the surface motion and around 10 m s^{-1} faster than the air motion at the level of the cirrus shield. This propagation speed is typical of the great speed of internal gravity waves, increasing the probability that this depression in the cirrus shield was caused by gravity wave motions.

To further verify that this depression in the cirrus shield was an effect of gravity wave activity, wind sets were generated at the level of the cirrus shield from which divergence fields were derived. The wind sets were obtained by the cloud tracking method, using the Man-computer Interactive Data Access System (McIDAS) of the University of Wisconsin Space Science and Engineering Center. A brief description of the cloud tracking procedure can be found in Suchman and Martin (1976). Suchman and Martin (1976), in their study of cloud motion winds during the GARP Atlantic Tropical Experiment (GATE), also found that cloud motion winds can describe the real wind field to within the accuracy of conventional techniques.

Because individual cloud features were often hard to distinguish on the full resolution (picture element size: 1/2 nautical mile) visible images, these images were filtered with a high-pass digital filter. This filter removes the low spatial frequencies in each digital image, enhancing the smaller scale detail. Therefore, it tends to remove the monotonic trend in brightness due to large-scale effects and brings out the smaller scale features, making the tracking of these features easier. The filtering did bring out an appreciable amount of detail, as is shown in Figure 9. Because the filtering technique changes the original digital data of each image, it

was necessary to track cloud elements by using the single pixel method (Suchman and Martin, 1976), rather than correlating cloud features on consecutive images.

After the wind sets were generated, the divergence fields were derived using the WIND*SRI computer program (Manusco and Endlich, 1973), producing the grid-point analysis of the divergence field for each period shown in Figure 10. In these computations, four winds were used for each grid-point calculation, and only winds within 0.5° latitude and longitude of a grid-point were selected for the computation of a value at that grid-point. Suchman and Martin (1976) found that, although divergence fields from SMS-obtained winds may not be wholly reliable quantitatively, that these fields are reliable and consistent in their qualitative aspects. Still, the mean magnitude of the divergence was about 2×10^{-4} s^{-1}, which is reasonable for a gravity wave with an amplitude such as that found for the surface gravity wave under study.

Figure 10 shows a general area of divergence ahead of the cloud depression for each time period, especially the last two. This relationship seems consistent with gravity wave theory. In fact, the agreement between the 2300 GMT location of the cloud depression and the 2245 GMT divergence pattern is quite remarkable; the depression moves into the exact area where divergence existed fifteen minutes earlier. Because of the agreement between these analyses and their consistency with theoretical characteristics of gravity waves, it is concluded that the depression in the top of the cirrus shield was the result of gravity wave motions.

4. Vertical Coupling of Observations

There was a strong resemblance between the observations of the surface gravity wave and the gravity wave aloft. Both were oriented in a northwest-to-southeast direction, and each was observed as only a low pressure trough. The propagation speeds of the two waves were nearly equal, and both were of relatively large amplitude. These similarities suggest that the surface and the upper level observations were actually observations of the same gravity wave, a gravity wave existing through a large depth of the troposphere.

This conclusion has important implications concerning the energy source of the wave. Figure 11 illustrates a vertical cross-section of the gravity wave at 2330 GMT. The wave was tilted toward the southwest with height, as it was at the other times of analysis. The magnitude of the slope was about 1:5. Because the horizontal phase speed was toward the northeast, this tilt would require an upward phase velocity component. The dispersion relationship for gravity waves is $\omega^2 = \omega_b{}^2 k^2 (k^2 + m^2 + (\frac{g}{2c_s})^2)^{-1}$, where ω is the frequency of the gravity wave, ω_b is the Brunt-Vaisalla frequency, k is the

horizontal wave number, m is the vertical wave number, g is gravity, and c_s is the speed of sound. The vertical trace speed is $c_z = \frac{\omega}{m} = \frac{\omega_b k}{m} (k^2 + m^2 + (\frac{g}{2c_s})^2)^{-1/2}$. The vertical group velocity, or the velocity at which the energy of the wave moves, is $c_{gz} = \frac{\partial \omega}{\partial m} = - \omega_b km(k^2 + m^2 + (\frac{g}{2c_s})^2)^{-3/2}$.

The vertical component of the phase velocity will have a sign opposite that of the vertical group velocity, meaning that they will be opposite in sense. For this study, therefore, the vertical group velocity was downward in direction, implying an upper level energy source. This tilt was also responsible for a pattern in which the rising motions, which occur behind the lowest pressure, and the pressure minimum at higher levels will coincide. This means that the product of the perturbation pressure and the perturbation vertical motion was negative, implying a downward energy flux, which is consistent with the previous statement.

The gravity wave has a large amplitude at upper levels for the period analyzed in Figure 8. This large amplitude was observed for a fairly long period despite the absence of strong trapping mechanisms at that level. Lindzen and Tung (1976) show that the tropopause, which is the most obvious trapping mechanism, is not a good reflector and, therefore, is not an effective trapping mechanism. Because the energy in an internal gravity wave propagates freely from the energy source, this large amplitude could exist only if this part of the wave was in the vicinity of the source region, although there was probably a horizontal advection of the energy by the upper level flow. According to Mastrantonio, et. al. (1976), upper level jet streams are capable of gravity wave initiation, since they possess kinetic energy in substantial amounts. The gravity waves are probably initiated as an adjustment response to ageostrophic motions within the jet stream. Because the energy source for the wave seems to be in the upper level of the troposphere, and because there existed a strong jet stream on 27 March, it appears that the jet stream was a likely source mechanism for the observed gravity wave. It must be noted, however, that this conclusion cannot be confirmed without more research, using a more complete data set (i.e., information concerning the wave at intermediate levels).

5. Summary

On 27 March 1975, gravity wave activity contributed greatly to local surface weather events in the midwestern United States, affecting both the pressure and wind fields. The surface gravity wave was investigated using surface barograph traces and hourly wind observations. In addition, SMS-I images were used to obtain information concerning the wave in the upper troposphere. Together, these observations indicate that the gravity wave was tilted with height. This finding, combined with the direction of propagation of the wave, implies that the wave possessed an upper level energy source. Because of the existence of a strong upper level jet stream prior

to and during the wave event, as was noted in other studies (Brunk, 1949; Tepper, 1951; Eom, 1975; Uccellini, 1975), it appears likely that the source mechanism of the gravity wave in this case was the adjustment associated with the propagating jet stream.

It is concluded that satellite-obtained data can be useful in the study of subsynoptic gravity waves. The features derived from SMS-I images were valuable in increasing the scope of understanding of the gravity wave in this study. It is realized that more research is required. There are many possibilities for increasing the data bases used. The addition of supplementary data at intermediate levels would have contributed greatly; this data could be obtained using balloons which remain on surfaces of constant pressure. Also, the use of ceilometer records, which could show areas of cloud dessication (Tepper, 1951), might prove valuable. These records were not available for this study, however, since the National Weather Service requires its stations to keep ceilometer records for only 90 days. More frequent observations from satellites would add much to the temporal resolution and consistency of the study. Finally, dynamics could be applied to initial data sets either to check their consistency or to add intermediate values to these sets. A new study, utilizing any or all of these suggestions, should result in more quantitative findings and have a considerable impact in contributing to the knowledge of gravity waves in the atmosphere.

ACKNOWLEDGEMENTS

I would like to thank all of the people without whose assistance this report would not have been written. I must express my sincere appreciation to Professor Verner E. Suomi for his help and encouragement throughout the duration of this research and for giving me the opportunity to do such a study. Professor John A. Young was instrumental in bringing the topic to my attention, in spending time answering questions, and in suggesting revisions to this work.

Many others contributed greatly during the course of this study. I am very grateful to Louis Uccellini for the interest that he showed in this work and the many discussions we had concerning it. I must thank Dr. Barry Hinton, Dr. Sanjay Limaye, Frederick Mosher, and J. T. Young for the advice and aid that they provided, especially concerning the work done on McIDAS. John Stremikis supplied some much appreciated help in the drafting of some figures. Finally, I would like to thank Katherine Shervis for her perserverence and time spent in obtaining large amounts of data from Asheville, N.C., for this study.

This research was funded by NASA Contract NAS5-24136 and by NOAA Grant 04-3-158-61.

The report was submitted as a thesis in partial fulfillment of the requirements for the degree of Master of Science (M.S.) in Meteorology at the University of Wisconsin-Madison, 1977.

REFERENCES

Brunk, I.W., 1949: The pressure pulsation of April 11, 1944. J. Meteor., 6, 395-401.

Eom, J., L975: Analysis of the internal gravity wave occurrence of April 19, 1970 in the Midwest. Mon. Wea. Rev., 103, 217-226.

Ferguson, H.L., 1967: Mathematical and synoptic aspects of a small scale wave disturbance over the lower Great Lakes area. J. Appl. Meteor., 6, 523-529.

Goldie, A., 1925: Waves at an approximately horizontal surface of discontinuity in the atmosphere. Quart. J. Roy. Meteor. Soc., 51, 239-246.

Lindzen, R.S., and K.-K. Tung, 1976: Banded convective activity and ducted gravity waves. Mon. Wea. Rev., 104, 1602-1617.

Manusco, R.L., and R. M. Endlich, 1973: User's Manual, Wind Editing and Analysis Program: Spherical Grid. WEAP-1A. Stanford Research Institute.

Mastrantonio, G.F., F. Einaudi, D. Fua, and D.P. Lanas, 1976: Generation of gravity waves by jet streams in the atmosphere. J. Atmos. Sci., 33, 1730-1738.

Suchman, D., and D.W. Martin, 1976: Wind sets from SMS images: An assessment of quality for GATE. J. Appl. Meteor., 15, 1265-1278.

Suomi, V.E., Principal Investigator, 1975: Man-computer Interactive Data Access System (McIDAS). Final Report. Contract NAS5-23296, University of Wisconsin, Madison.

Tepper, M., 1951: On the dessication of a cloud bank by a propagated pressure wave. Mon. Wea. Rev., 79, 61-70.

Uccellini, L.W., 1975: A case study of apparent gravity wave initiation of severe storms. Mon. Wea. Rev., 103, 497-513.

Wiin-Nielsen, A., 1965: On the propagation of gravity waves in a hydrostatic, compressible fluid with vertical wind shear. Tellus, 17, 306-320.

Young, J.A., 1975: Class notes; University of Wisconsin-Madison.

Young, J.A., and C. F. Richards, 1973: A climatological study of surface pressure events at Madison, Wisconsin: Preliminary results relating to possible gravity wave activity. Proj. Rep. NG-26-72, University of Wisconsin, Madison, 172-187.

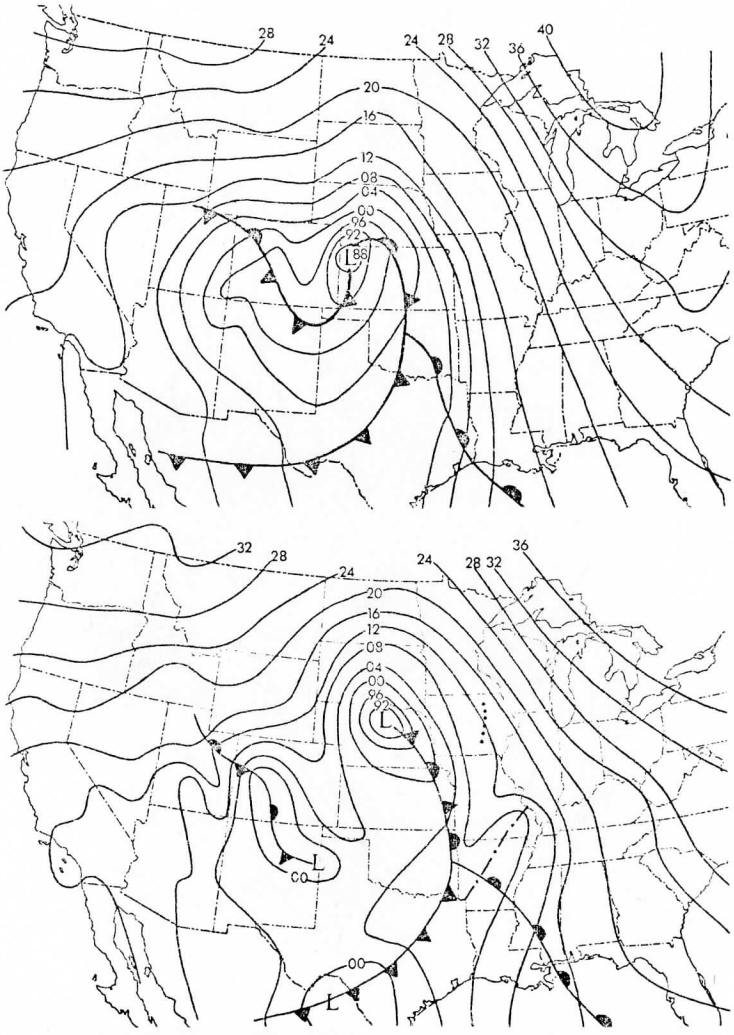

FIGURE 1: Sea level pressure analyses for 1200 GMT 27 March 1975 (above) and 2100 GMT 27 March 1975 (below). Maps are analyzed for every 4 mb. Dotted line on lower chart is the axis of the surface pressure anomaly at 2100 GMT.

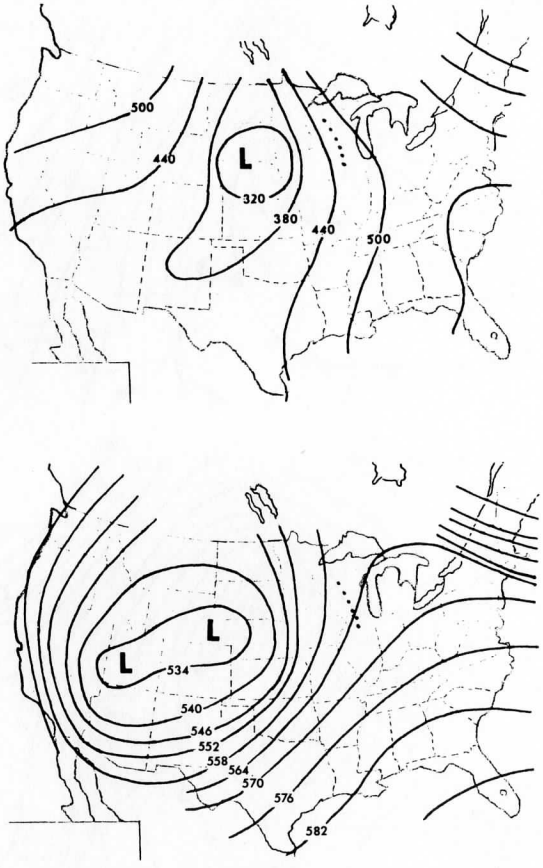

FIGURE 2: Analyses at 850 mb (above) and 500 mb (below) for 0000 GMT 28 March 1975. Maps are analyzed for every 60 geopotential meters. Dotted line represents the axis of the surface pressure anomaly at 0000 GMT.

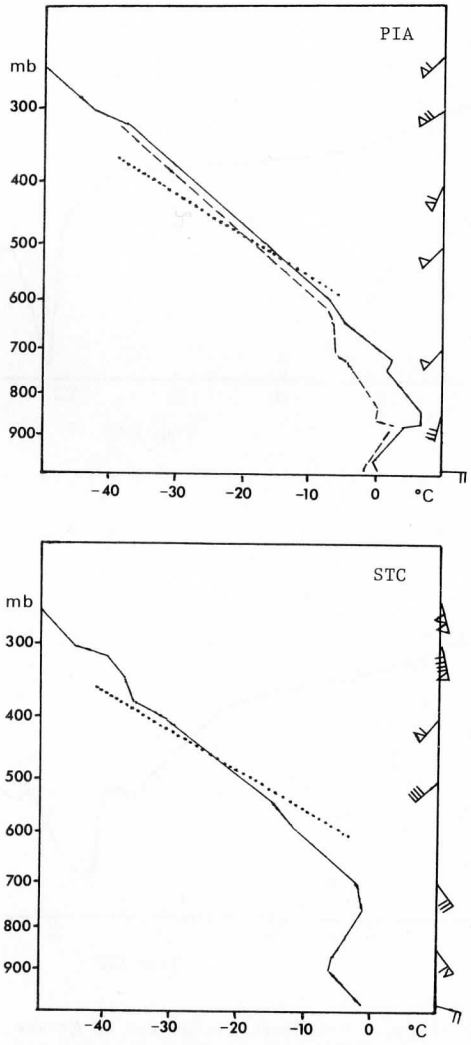

FIGURE 3: Atmospheric soundings for Peoria, Illinois (PIA) and St. Cloud, Minn. (STC) at 0000 GMT 28 March 1975. Solid lines represent the air temperature, dashed lines the dew-point temperature and dotted lines the dry adiabats. At right are winds at standard pressure levels. Moisture data was not available for St. Cloud.

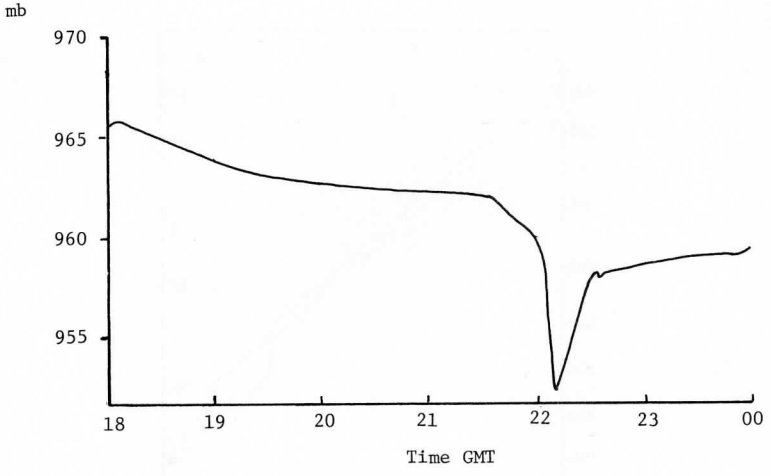

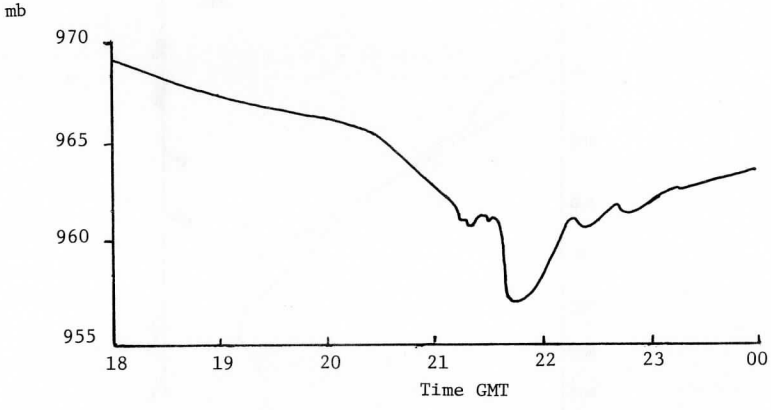

FIGURE 4: Surface barograph traces for La Crosse, Wisc. (above) and Rochester, Minn. (below). The traces are for the time interval from 1800 GMT 27 March 1975 until 0000 GMT 28 March 1975.

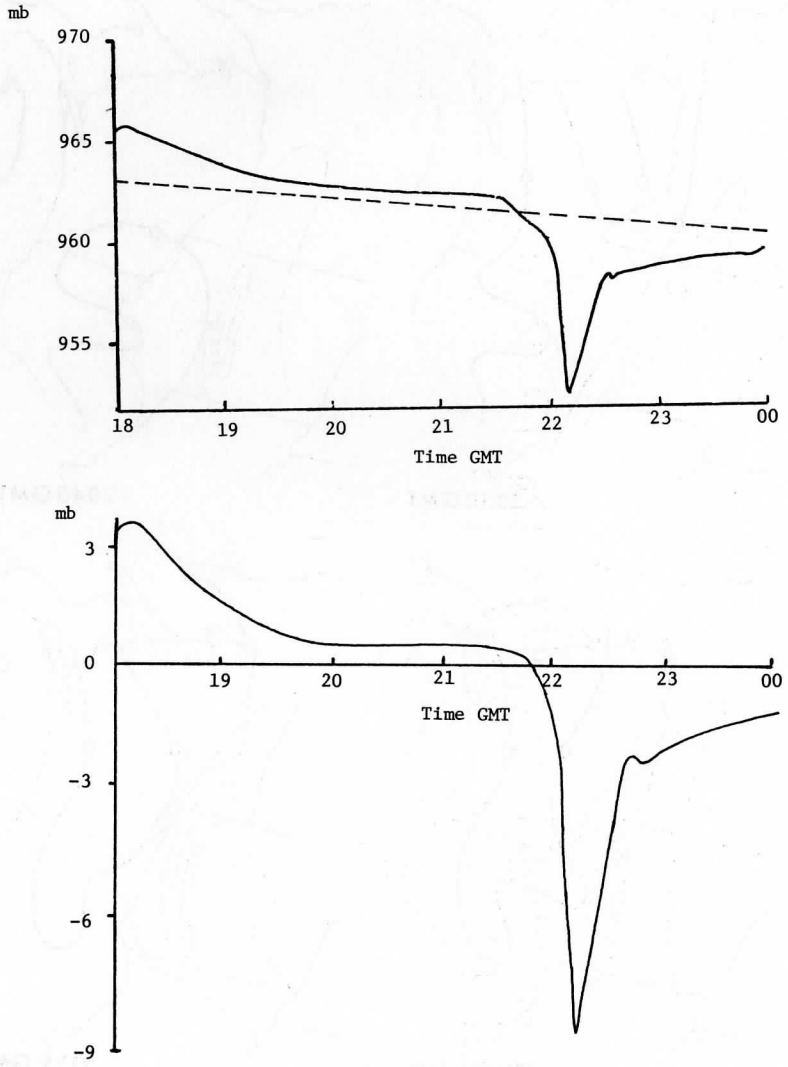

FIGURE 5: Sample of perturbation pressure analysis. Original trace of La Crosse, Wisc. (above), with least-squares linear trend approximation (dashed line). Pressure perturbation trace is below.

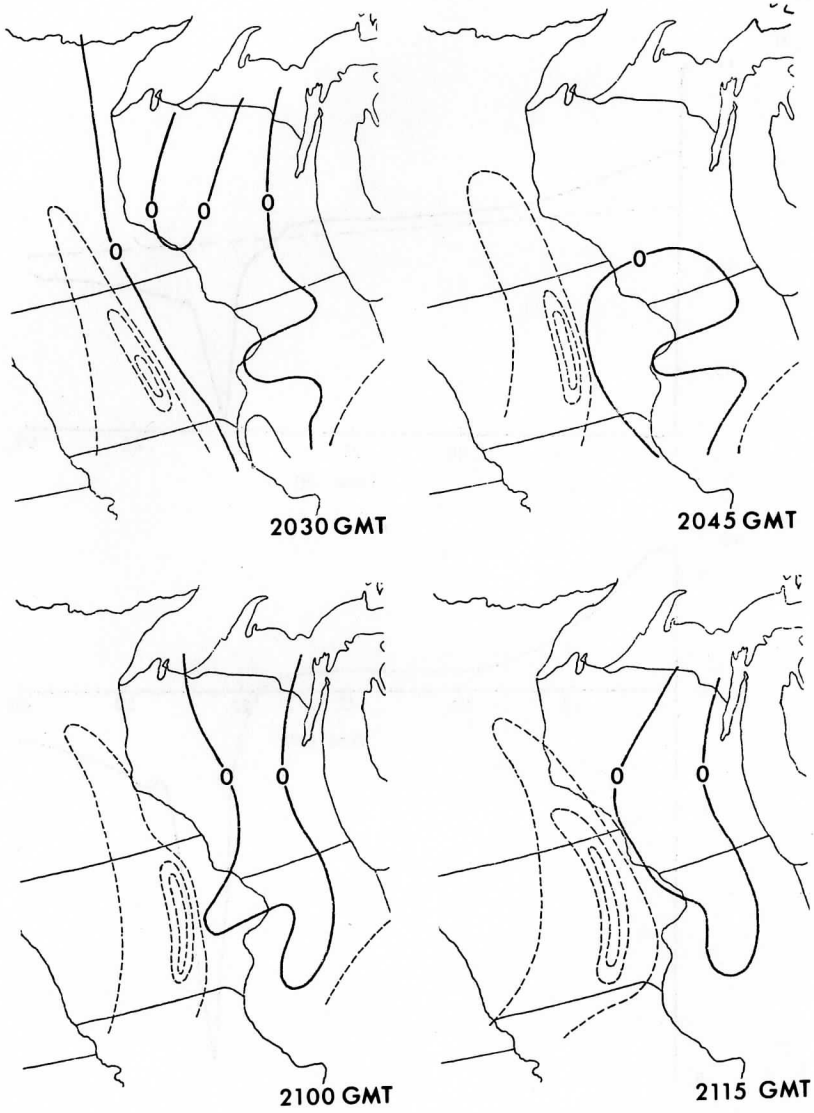

FIGURE 6.a: Successive perturbation pressure (p') maps analyzed at 1.7 mb (0.05 in. Hg) intervals. Negative p' shown as thin dashed lines; positive p', thin solid lines; p' = 0, thick solid lines.

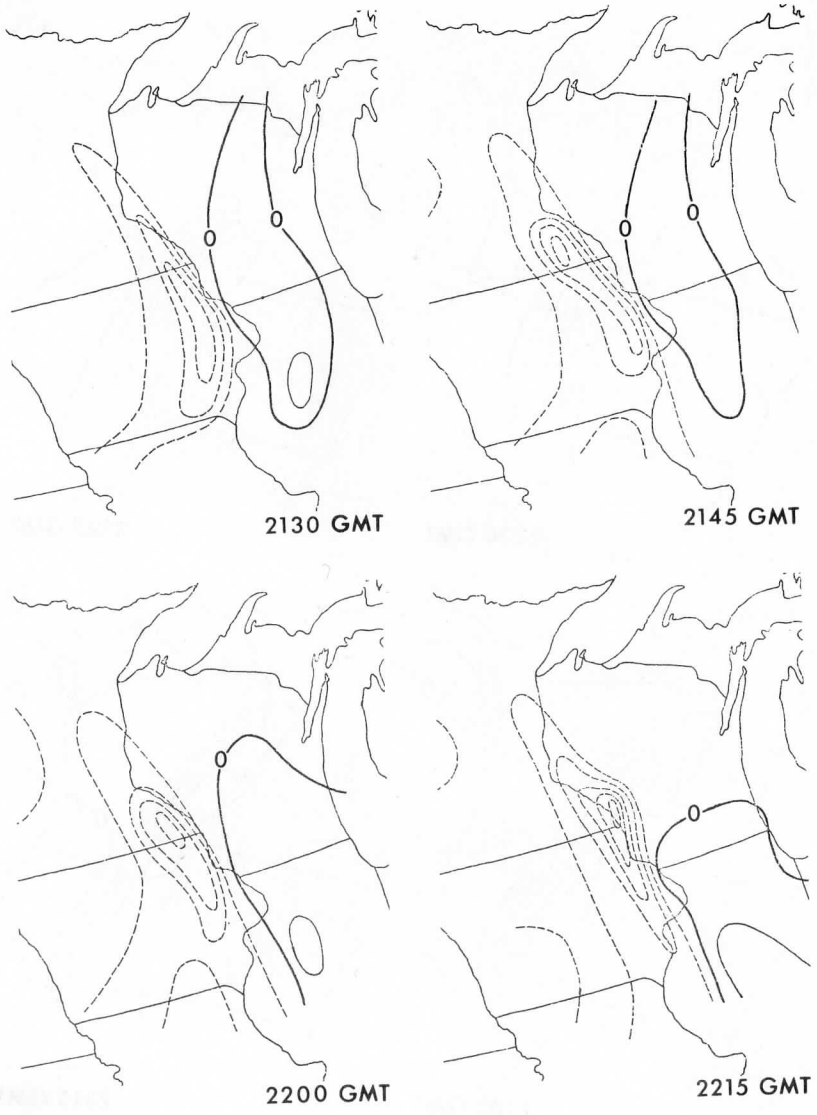

FIGURE 6.b: Same as Figure 6.a, but for different analysis times.

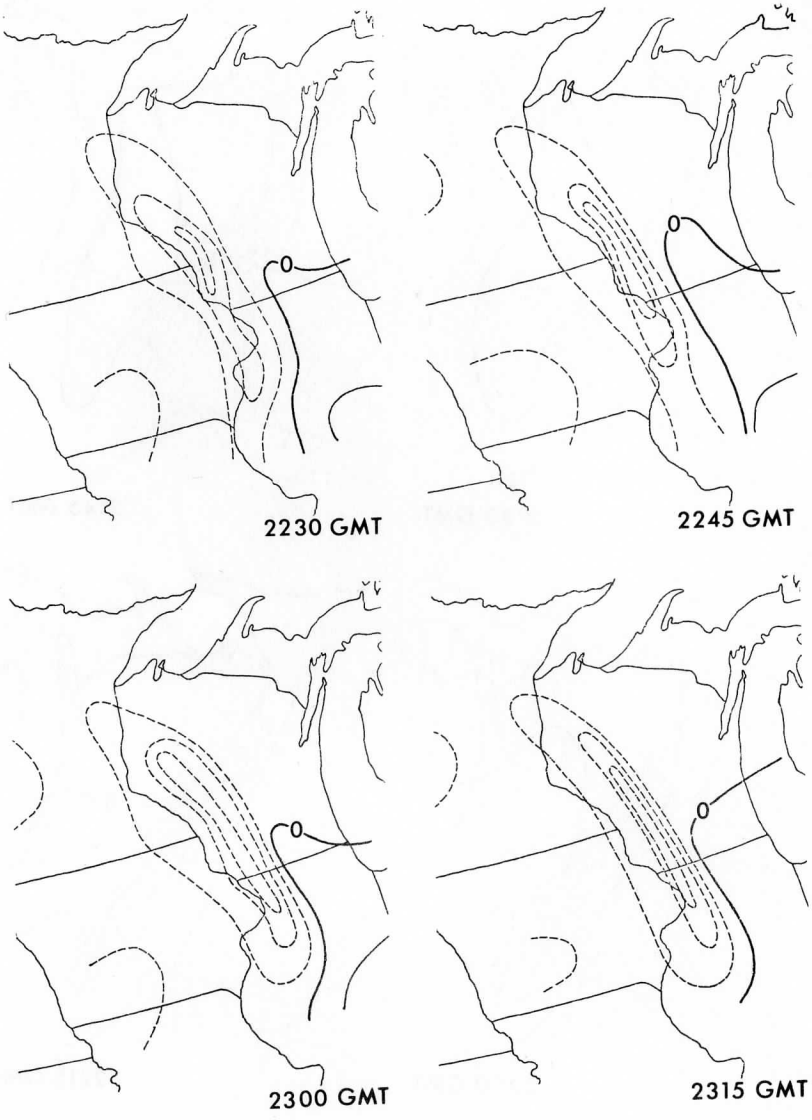

FIGURE 6.c: Same as Figure 6.a, but for different analysis times.

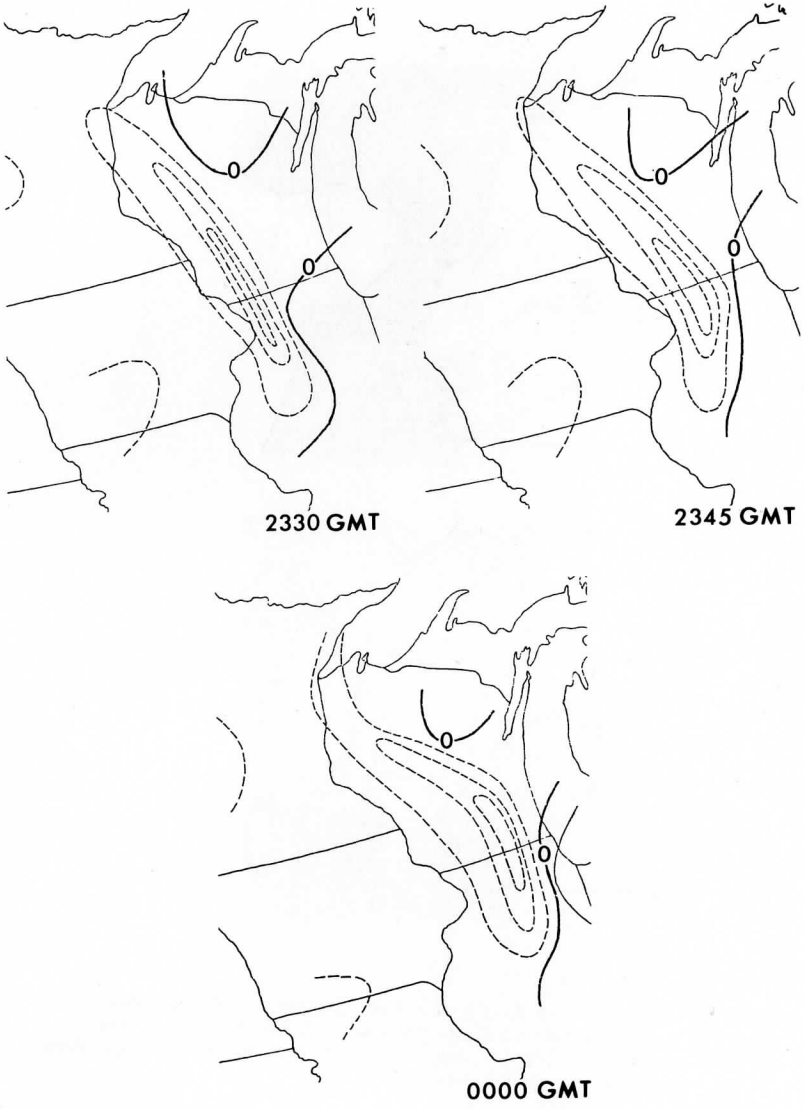

FIGURE 6.d: Same as Figure 6.a, but for different analysis times.

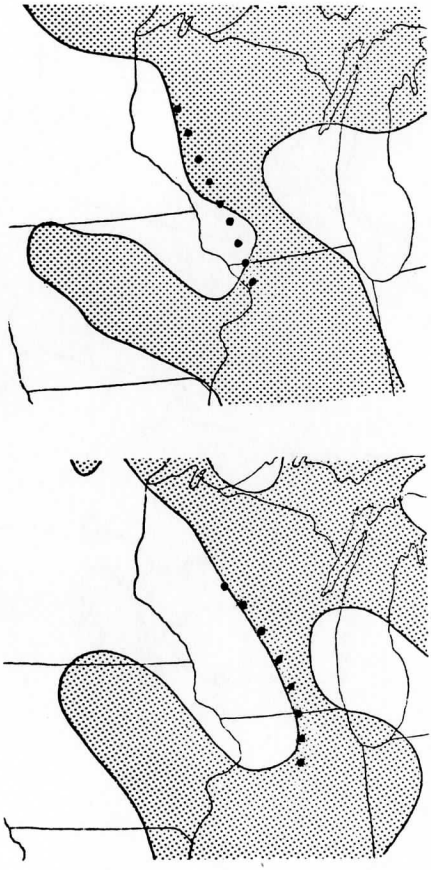

FIGURE 7: Surface wind divergence for 2300 GMT 27 March (above) and 0000 GMT 28 March (below). Divergent areas are shaded. Dotted lines represent axis of surface pressure anomaly at each time.

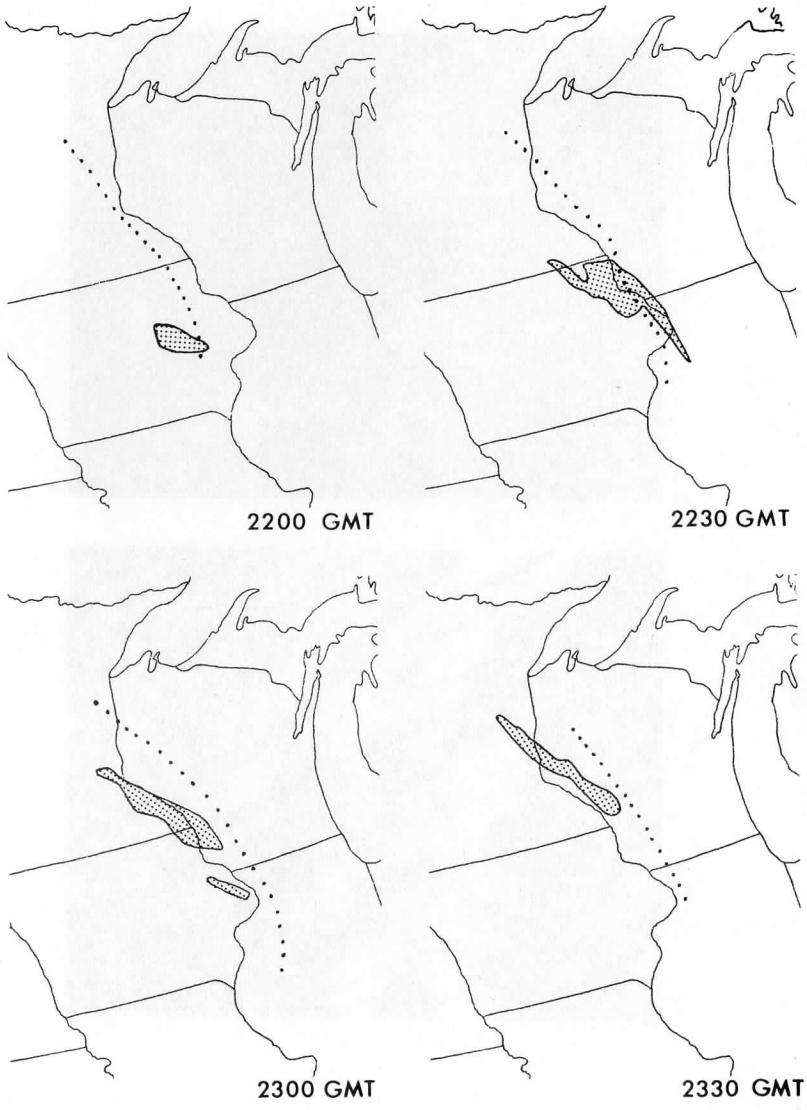

FIGURE 8: Outline of depression in cirrus shield. The shaded area denotes that part of the cirrus shield that was warm relative to its surroundings. Dotted lines represent the axis of the surface gravity wave at each time.

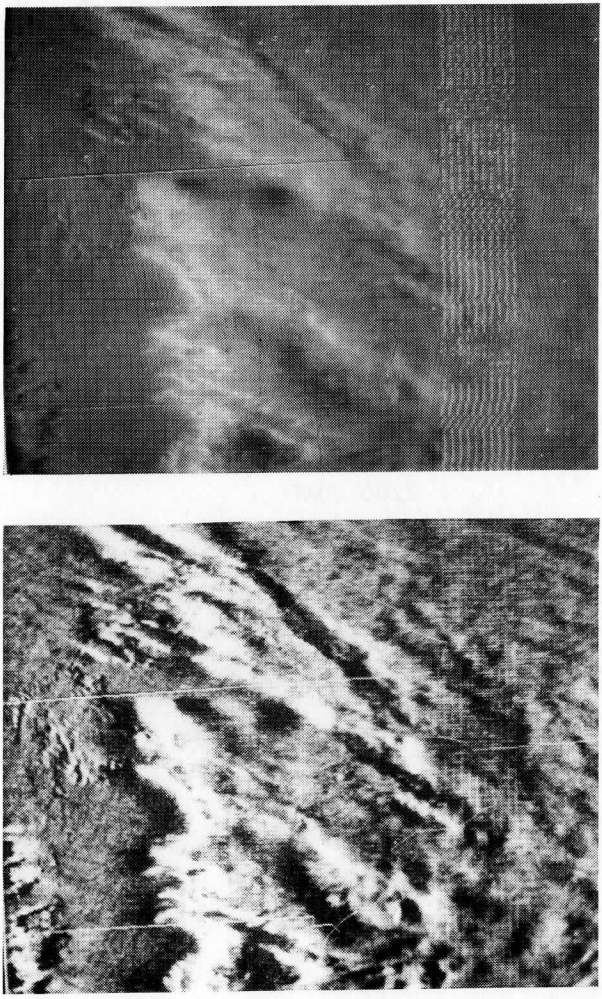

FIGURE 9: Example of image filtering process for 2300 GMT image. Above is unfiltered visible image, below is filtered visible image. Dotted lines right of center are caused by a flaw in the data archive.

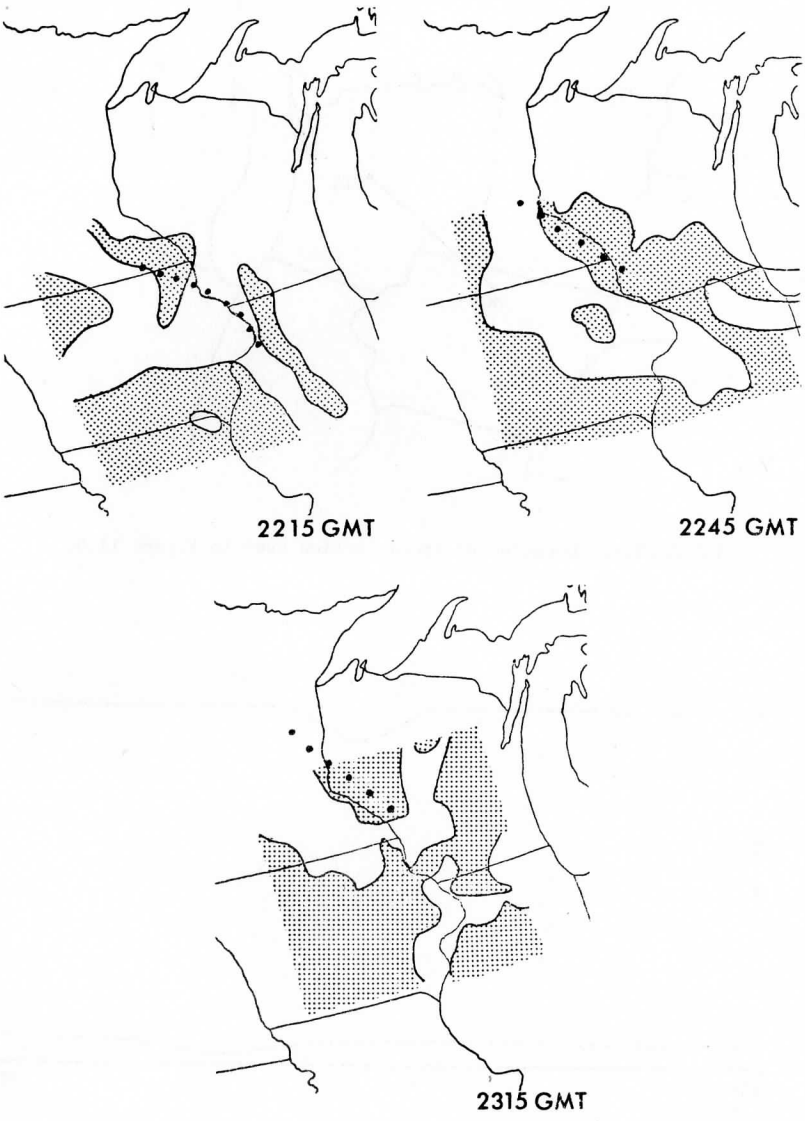

FIGURE 10: Divergence at level of cirrus shield. Divergent areas are shaded. Dotted lines represent the axis of the cirrus shield depression 15 minutes after the analysis. The analyses cover only that area where satellite winds were obtained.

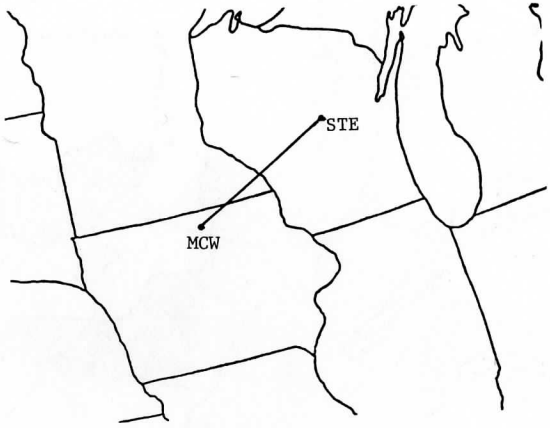

FIGURE 11.a: Location of cross-section used in Figure 11.b.

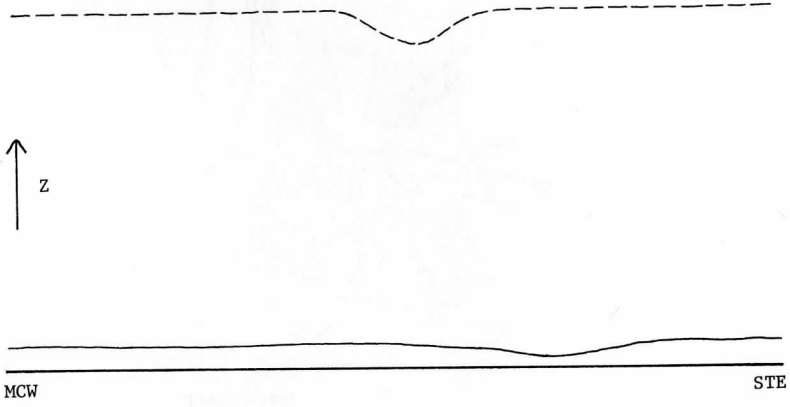

FIGURE 11.b: Vertical cross-section from Mason City, Iowa (MCW) to Stevens Point, Wisc. (STE) for 2330 GMT 27 March 1975. The solid line represents a pressure surface at lower levels. The dashed line represents an isentropic surface at higher levels which depict the cloud depression.

APPENDIX A

Gravity Wave Theory

Throughout the period in which the gravity wave was observed, its form remained the same. This allows the use of the "frozen" traveling anomaly pattern theory (Young, 1975). Perturbation fields are a function of (x-ct), where x is the direction in which the disturbance is traveling, c is the phase speed in the x-direction, and t is time.

If u' and v' are the wind perturbations in the x- and y-directions, respectively, f is the coriolis parameter, $\overline{\rho}$ is the mean density, and p' is the pressure perturbation, then the linearized equations of motion may be expressed as equations (1) and (2):

$$\frac{\partial u'}{\partial t} + \overline{u}\frac{\partial u'}{\partial x} - fv' = -\overline{\rho}^{-1}\frac{\partial p'}{\partial x} \tag{1}$$

$$\frac{\partial v'}{\partial t} + fu' = 0 \tag{2}$$

Because simple gravity wave motions are being considered, the small time and space scales allow the dropping of the coriolis-related terms. Consequently, the equations of motion then reduce to (3) and (4):

$$\frac{\partial u'}{\partial t} + u\frac{\partial u'}{\partial x} = -\rho^{-1}\frac{\partial p'}{\partial x} \tag{3}$$

$$v' = 0 \tag{4}$$

Because ρ' and u' are functions of (x-ct), equations (5) and (6) hold:

$$\frac{\partial p'}{\partial x} = -c^{-1}\frac{\partial p'}{\partial t} \tag{5}$$

$$\frac{\partial u'}{\partial x} = -c^{-1}\frac{\partial u'}{\partial t} \tag{6}$$

Relating (5) and (6) to equation (3) for the u-component, we find (7):

$$\frac{\partial u'}{\partial x} = [\overline{\rho}\ (c - u)]^{-1}\frac{\partial p'}{\partial x} \tag{7}$$

From this, equation (8) then follows:

$$u' = \frac{p'}{[\overline{\rho}\ (c - u)]} \tag{8}$$

Finally, we may then express $\frac{\partial u'}{\partial x}$ in terms of either equation (9) or equation (10):

$$\frac{\partial u'}{\partial x} = [\overline{\rho}\ (c - u)]^{-1}\ \frac{\partial p'}{\partial x} \qquad (9)$$

$$\frac{\partial u'}{\partial x} = -[\overline{\rho}c\ (c - u)]^{-1}\ \frac{\partial p'}{\partial t} \qquad (10)$$

These equations provide a link between the horizontal divergence and the perturbation pressure tendency at any level. They show that divergent motions must precede the pressure trough of a gravity wave; i.e., they must coincide with the area where the pressure is falling.

Because of the tilt of the wave and the divergent motions ahead of the wave trough, there will be downward vertical motion ahead of the upper level wave trough, causing a depression-like feature in isentropes at that level. This is shown schematically in Figure A.1.

The divergence associated with the wave trough at lower levels occurs under an area that is free of the influence of the higher level wave trough. At this upper level, though, downward motions are forced to compensate for the divergence below. Behind the wave trough, there will be rising motions at almost all levels, due to convergent motion behind the wave trough. This causes a distortion of the isentropes at upper levels (see Figure A.1), with a depression-like feature ahead of the upper level wave trough.

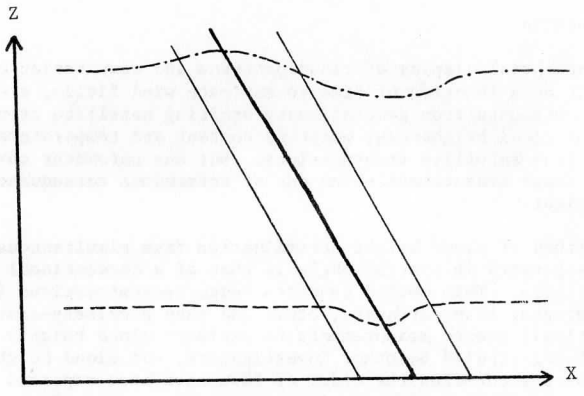

FIGURE A.1: Schematic vertical cross-section of wave. Wave is moving left to right. Thick solid line is the wave trough axis, thin solid lines are the boundaries of the influence of the pressure perturbation in the horizontal plane, with divergence ahead of the trough and convergence behind. Dashed line is a low level pressure surface, dot-dashed line is an upper level isentropic surface.

Cloud Height Determination from Multiple Geostationary Satellite Images using a Computer Video Display System

William R. Bryson

ABSTRACT

This report describes a technique for the determination of the heights of clouds displayed in overlapping images transmitted from two geostationary satellites.

1. Introduction

The sequential display of cloud patterns and computation of cloud displacement as a function of time to estimate wind fields, are now fairly routine measurements from geostationary orbiting satellite transmissions. Estimates of cloud brightness, moisture content and temperature are also obtainable from satellite transmissions. But one parameter obviously missing in these measurements--and one of tremendous consequence--is that of cloud height.

One method of cloud height determination from simultaneous views which are separated in spatial angle is that of a conventional stereographic analysis. This method requires image reconstructions (e.g., hard-copy photographs, transparencies, etc.) and then precisely-controlled visual (optical) stereo measurements to estimate cloud heights. This method is being studied by other investigators, and cloud height determinations with accuracies the order of 500m have been reported using selected photographs of high resolution from the Apollo VI mission [Shenk et. al. 1975], and selected SMS photographs [Minzner and Shenk 1977]. The Apollo VI photographs were obtained using a high-quality camera from a lower satellite orbit than is considered in this work. Current geostationary satellite transmissions are digital and photographic reconstructions are limited to resolutions poorer than high-resolution photographs. This method also is not compatible with routine computer processing such as wind speed determination and cloud temperature measurements.

The method which is reported here makes the cloud height measurements using computed triangulation measurements with cross-correlation techniques and with the support of existing computer navigation subroutines. One advantage of this method is the direct use of satellite data (in digital format) without the need for photo reconstructions. It also interfaces with existing subroutines available at the UW Space Science and Engineering Center for navigation, wind measurements and graylevel enhancements.

2. Geometrical Description

The geometry of two satellites located in geostationary orbits which are inclined at angles ϕ_A, ϕ_B, respectively, to the equatorial plane is depicted in Fig. 1. For convenience, satellite S_B is assumed to be located to the west of satellite S_A. The satellite subpoints are designated by SA_{SP}, SB_{SP}, respectively.

Let P be a point of interest on the earth's surface which lies within the field of view of both satellites. The north-south angle from the equatorial plane to point P is designated by ξ and the east-west angle from the polar plane which includes the subpoint SB_{SP} is designated by ψ. These angles also are shown in Fig. 1.

An oblate spherical earth is assumed and an east-west angular separation between satellites on the order of 60° is considered typical. (The satellites are separated by 32° in the currently available data: day 48, 1975.)

The projection of the two-satellite viewing area on the earth's surface from point SA_{SP} to point SB_{SP} and from 30°N to 30°S is depicted in Fig. 2. The spatial mapping from the coordinates of a spin-stabilized geostationary orbiting satellite to earth coordinates is approximately linear for nadir angles less than 30°. For larger angular displacements, some mapping corrections are necessary. These mapping corrections are known, however, and can be incorporated in the computer subroutines. (Parent 1974; Phillips and Smith 1974).

The area of primary concern for this analysis lies within the rectangular area shown in Fig. 2. As a result of symmetry, it is sufficient to consider only one-fourth of this area, which is shown as the shaded area in Fig. 2. For convenience, it is assumed--unless stated otherwise--that the point P lies in the vicinity of that polar plane which is midway between the two satellites. This restriction keeps the required mapping corrections to a minimum. The effects of more extensive mapping corrections are straight forward and can be incorporated at a later time.

3. Measurement Basis

The measurement basis of this cloud-height analysis technique relies heavily on the "navigation" of SMS images, performed by the McIDAS system at SSEC. McIDAS stands for Man-computer Interactive Data Access System, and the design and operation of the system for image navigation is described by Chatters and Suomi (1975), Smith (1975), and Phillips and Smith (1973).

The inherent stability of the SMS geostationary satellite platform and the geometrical fidelity of the VISSR (Visible/Infrared Spin-Scan Radiometer) aboard the satellite make computerized image navigation (via McIDAS) possible.

The first step in the measurement is the determination of the locations of the two satellites in an earth-centered, XYZ coordinate system. These

locations are available from the navigation procedures. Let the location of S_B, the more western satellite, be p,q,r and let the location of S_A, the more eastern satellite, be s,t,u.

Next, a cloud of interest is selected by the McIDAS analyst by placing a cursor box over the cloud on a TV display of the eastern satellite image data. Using the center of the cursor as "the location" of the cloud, denoted as P_A, the navigation routines are again called upon to provide the XYZ coordinates of the point. This location, (denoted l,m,n), is treated as though it lies on the surface of the earth.

It is then necessary to go to the data from the more western satellite, S_B. This data cannot be used directly, but must be remapped into a form suitable for cross-correlation with S_A's data. Rather than remap the data of both S_A and S_B to a common plane as suggested by Minzner et. al. (1977), we simply remap that small area covered by the cursor from the sphere as seen by S_B to the sphere as seen by S_A. This reduces the amount of degradation of the data as compared to mapping to a common plane. (See section 5 for a more extensive discussion of the necessity for remapping and problems associated with it.)

Two dimensional cross-correlation analysis is utilized in determining the apparent parallax of the cloud selected for study earlier. A 32 row by 32 element image grid (the cursor size used above) containing the selected cloud is cross-correlated at all possible lag positions with a 64 row by 64 element image grid from the second picture. The result is a 33 x 33 cross-correlation matrix which includes the 0,0 lag position as its center. The cross-correlation matrix is then searched for its maximum value. The lag position of this maximum is then used as the apparent parallax of the cloud. Let $\bar{\Gamma}$ represent the vector from the zero lag position to the max lag position, with magnitude γ. To increase resolution, a bi-directional quadratic is fit to a neighborhood of the maximum coefficient. This interpolation allows the selection of non-integral lag positions.

We are now ready to compute the altitude of our cloud. First, we compute the vector from S_A to P_A, called $\overline{SAP}$, and the vector from S_B to P_A, called $\overline{SBP}$

$$SAP = (p - l)\hat{i}, (q - m)\hat{j}, (r - n)\hat{k} \tag{3.1}$$

$$SBP = (s - l)\hat{i}, (t - m)\hat{j}, (u - n)\hat{k} \tag{3.2}$$

Next, the normal to the tangent plane to the earth at point P_A is found. If an oblate spheroidal earth is assumed with polar radius a and equatorial radius b, it can be expressed as:

$$\frac{x^2 + y^2}{b^2} + \frac{z^2}{a^2} = 1 \tag{3.3}$$

The normal vector at point P_A (1,m,n) is found by applying the ∇ operator at point P_A.

$$\bar{N}_{P_A} = \nabla\left(\frac{x^2}{b^2} + \frac{y^2}{b^2} + \frac{z^2}{a^2} - 1\right) \tag{3.4}$$

and substituting 1,m,n for x,y,z, resulting in

$$\bar{N} = \frac{1}{b^2}\hat{i}, \frac{m}{b^2}\hat{j}, \frac{n}{a^2}\hat{k} \tag{3.5}$$

Next, the normal to the plane including the points S_A, S_B and P_A is found. This is simply the cross product between $\overline{SAP}$ and $\overline{SBP}$. Then, the intersection line of the tangent plane and the plane including S_A, S_B and P_A is

$$(\overline{SAP} \times \overline{SBP}) \times \bar{N} = (\overline{SBP} - \bar{N})\overline{SAP} - (\overline{SAP}\ \bar{N})\overline{SBP} = \bar{\Gamma}_c \tag{3.6}$$

It is now apparent that there are two means of obtaining the direction of the apparent parallax vector. The first is measured by the cross-correlation peak. The second is the direction of the intersection vector of the earth tangent plane and the plane including points S_A, S_B and P_A. This will provide a quality control check on the validity of the cross-correlation step.

Assuming reasonable agreement between the two methods above the apparent location of the cloud, as seen by satellite B, (the more eastern satellite) can be defined. This is done by moving an amount γ from P_A in the direction of $\bar{\Gamma}_c$. Let P_B, (d,e,f) represent this point. Now define a vector from S_B to P_B; let this vector be $\overline{SPB}$. By the definition of P_B, we know that vectors $\overline{SAP}$ and $\overline{SPB}$ will intersect. Now, a line through a point, S_A, and parallel to the vector, $\overline{SAP}$, is

$$\frac{x - p}{SAP_x} = \frac{y - q}{SAP_y} = \frac{z - r}{SAP_z} \tag{3.7}$$

The line through S_B and parallel to SPB can be found in the same way, resulting in

$$\frac{x - s}{SPB_x} = \frac{y - t}{SPB_y} = \frac{z - u}{SPB_z} \tag{3.8}$$

If the point of intersection of the lines expressed in 3.7 and 3.8 is

denoted as T, then the x, y and z components of T are:

$$x_T = \frac{AD(y_2 - y_1) + BDx_1 - AEx_2}{AE - BD} \tag{3.9}$$

$$y_T = \frac{BE(x_2 - x_1) + AEy_1 - BDy_2}{AE - BD} \tag{3.10}$$

$$z_T = \frac{FC(x_2 - x_1) + AFz_1 - DCz_2}{AF - CD} \tag{3.11}$$

where: x_1, y_1 and z_1 represent the x,y,z location of S_A; $x_2y_2z_2$ represent the location of S_B; and

$$A = (1 - p),\ B = (m - q),\ C = (n - r)$$

$$D = (d - s),\ E = (e - t),\ F = (f - u)$$

The last step in the procedure is to calculate the magnitude of the vector from the origin to T and subtract from this the magnitude of the vector from the origin to P_A. This yields the elevation of the cloud over a virtual earth surface, the oblate spheroid used in the navigation procedure. Finally, it is necessary to determine the difference in altitude between the virtual earth and the real earth. Since this difference is a well-behaved function, we can simply determine the elevation of a number of widespread control points and apply a correction factor.

4. Scaling Dependencies

The basic geometrical three-dimensional model was analyzed on a computer so that the effects of various parameter changes could be evaluated. Plots of several parameter variations are shown in Figs. 3, 4, and 5.

In Fig. 3, the north-south angular positions of the satellites, ϕ_A, ϕ_B, are permitted to vary in opposite directions from the equatorial plane. An overall angle, ϕ, is defined as $\phi = \phi_A - \phi_B$, and the point P is constrained to be in the equatorial plane and approximately midway between the two satellites. The distance γ is the apparent parallax of the cloud. The percent error in cloud height determination is defined by

$$\% \text{ ERROR} = \frac{\frac{\partial(\text{CLOUD HEIGHT})}{\partial\gamma}}{\text{CLOUD HEIGHT}} \times 100\% \tag{4.1}$$

To indicate the relative magnitudes, the cloud height h vs. the distance γ in the equatorial plane for an angular separation of 60° between the geostationary satellites is given in Table 1. Shown in Table 2 are cloud

heights vs. γ at a point 15° south and on the polar plane including SPB.

The plots in Figs. 3-5 show that the normalized determination of cloud height is relatively insensitive to small north-south satellite drifts from the equatorial plane (Fig. 3), to variations in the east-west angle from the subpoint of satellite S_A to the point of interest (Fig. 4), and to variations in the north-south angle from the subpoint of satellite S_A to the point of interest (Fig. 5). Data for all three plots were restricted to the shaded area shown in Fig. 2.

From preliminary considerations, and based upon experience with wind measurements using cross-correlation techniques, it appears that the cross-correlation peaks for "good" cloud patterns can be performed within one resolution element in the satellite data. (Phillips, 1977). Based on the scaling indicated in Tables 1 and 2 and on the resolution capabilities of current geostationary orbiting satellites, this would yield an error of cloud height determination of better than 500m. This is equivalent to an error of about 6 percent in pressure altitude.

5. Remapping

The need for remapping one image to the projection of the other is quite obvious when one wishes to view a common point from two satellites. The first correction is required by the rotational effect due to non-parallel spin axes of the two spacecraft. If not corrected this can result in a divergence of 25 lines in a span of 300 elements when two lines pass through a common point (see Fig. 6). Remapping is also needed to correct the foreshortening due to changes in scale as one moves away from the satellite subpoint.

The remapping of an image from the projection of satellite B to that of satellite A is, in its simplest form, quite straightforward. First, the latitude and longitude and longitude of each point in the satellite A image are determined. These latitude and longitude coordinates are then converted to line and element coordinates in satellite B image space, and the appropriate data point is transferred to an 'output area', or storage array for the remapped image. The drawback of this solution is the very large number of calculations required to perform point by point navigation transforms, but this drawback can be circumvented. It can be shown that if the line and element space of satellite A is divided into triangular subspaces, these subspaces will transform into a complete cover of satellite B's line and element space. (Phillips 1977)

Therefore, we first perform a navigation transform of each vertex of a triangular subspace (called S_1) in satellite A line and element space. If we denote these points as V_1, V_2, and V_3 (see Fig. 7) with coordinates $(L_{1A}E_{1A})$, $(L_{2A}E_{2A})$ and $(L_{3A}E_{3A})$, their corresponding latitudes and longitudes will be (Lat_1, Lon_1), (Lat_2, Lon_2) and (Lat_3, Lon_3). We now wish to transform the line and element coordinates of the points within the subspace without using the normal navigation transform procedure. If we solve the following sets of simultaneous equations for A and B we will arrive at the

desired result:

$$\begin{aligned} Lat_1 + A_{Lat}(L_{2A}-L_{1A}) + B_{Lat}(E_{2A}-E_{1A}) &= Lat_2 \\ Lat_1 + A_{Lat}(L_{3A}-L_{1A}) + B_{Lat}(E_{3A}-E_{1A}) &= Lat_3 \end{aligned} \tag{5.1}$$

and

$$\begin{aligned} Lon_1 + A_{Lon}(L_{2A}-L_{1A}) + B_{Lon}(E_{2A}-E_{1A}) &= Lon_2 \\ Lon_2 + A_{Lon}(L_{3A}-L_{1A}) + B_{Lon}(E_{3A}-E_{1A}) &= Lon_3 \end{aligned} \tag{5.2}$$

The latitude and longitude of any point within S_1 may now be found with the following transforms:

$$\begin{aligned} T[L_A,E_A \rightarrow Lat] &= Lat_1 + A_{Lat}(L_A-L_{1A}) + B_{Lat}(E_A-E_{1A}) \\ T[L_A,E_A \rightarrow Lon] &= Lon_1 + A_{Lon}(L_A-L_{1A}) + B_{Lon}(E_A-E_{1A}) \end{aligned} \tag{5.3}$$

Next we do a navigation transform for the points V_1, V_2, V_3 from latitude and longitude to satellite B line and element space, (L_{1B},E_{1B}), (L_{2B},E_{2B}) and (L_{3B},E_{3B}). By solving equations (5.1) and (5.2) with Lat substituted for L_A and Lon for E_A, we obtain the following transforms for points within the subspace:

$$\begin{aligned} T[Lat, Lon \rightarrow L_B] &= L_{1B} + A_L(Lat-Lat_1) + B_L(Lon-Lon) \\ T[Lat, Lon \rightarrow E_B] &= E_{1B} + A_E(Lat-Lat_1) + B_E(Lon-Lon) \end{aligned} \tag{5.4}$$

By combining the transforms of (5.3) and (5.4) we can go from satellite A line and element space to satellite B line and element space with a consequent reduction $\mathfrak{O}$ (nm) in the number of navigation transforms required where n and m are the base and height in elements and lines of the triangular subspaces.

6. Results to Date

The most dramatic use to date of the described technique has been the production of stereo cloud pictures. A 500 x 672 area of full resolution S_B data is first remapped to the projection as seen by S_A. The S_A data is then displayed on a tv monitor in green. The remapped S_B data is displayed on the same monitor in red. The result, when viewed thru glasses with one red lens and one green lens, is a very good three-dimensional effect. The problem of a nonlinear monitor is avoided because the single display used distorts both images in the same manner. When displayed in time sequences, both horizontal and vertical changes in the cloud layers can be observed in a satellite image. Fig. 8 illustrates, in picture pair format, the stereo capabilities.

A number of preliminary cloud height measurements have been made, using the techniques discussed earlier. These measurements tend to confirm that resolution of better then 500 m is possible, but the limited availability of satellite data to work with has severely hampered this work.

7. Future Work

A second satellite receiving system has been completed at the Space Science and Engineering Center and pairs of SMS/GOES images are now available on a daily basis. While these will not always be simultaneous pairs they will allow the determination of the elevation of geographical features and thus will provide a check on the true accuracy of the technique.

ACKNOWLEDGEMENTS

I would like to thank Dennis Phillips and Professors Verner E. Suomi and Ferrel G. Stremler for their continuing assistance and encouragement throughout this project. It is also a pleasure to acknowledge the fine cooperation of the many people at SSEC. This work was funded by NASA Grant NAS5-24136.

REFERENCES

Chatters, G. C. and V. E. Suomi, 1975: The Applications of McIDAS, IEEE Trans. Geosci. Electronics (GE-13), 137-146.

Minzner, R. and W. E. Shenk, 1977: Unpublished manuscript.

Parent, R. J., 1974: SMS data System analysis-position: A summary, in Studies of the Atmosphere Using Aerospace Probes 1973, Annual Rept., NOAA Grant NG-26-27, Space Science and Engineering Center, University of Wisconsin Press, Madison, WI 53706.

Phillips, D. and E. Smith, 1974: Geosynchronous satellite navigation model, in Studies of the Atmosphere Using Aerospace Probes 1973, Annual Rept., NOAA Grant NG-26-27, Space Science and Engineering Center, University of Wisconsin Press, Madison, WI 53706.

Phillips, D., and E. A. Smith, 1973: McIDAS Cloud tracking system, Goddard Space Flight Center Contract Report for NAS5-21794.

Shenk, W. E., R. J. Holub and R. A. Neff, 1975: Stereographic cloud analysis from Apollo 6 photographs over a cold front, Bull. Am. Met. Soc. (56), 4-16.

Smith, E. A., 1975: The McIDAS system, IEEE Trans. Geosci. Electronics (GE-13), 123-136.

Stremler, F. G., M. A. Khalil and R. J. Parent, 1977: Ground mapping resolution accuracy of a scanning radiometer from a geostationary satellite, Appl. Optics. (16), 1619-1627.

Table 1. Cloud height, h, as a function of parallax, γ.

γ (km)	h (km) target cloud midway between satellites	h (km) target cloud directly beneath one satellite
0	0	0
1	0.71	0.42
2	1.43	0.84
3	2.14	1.26

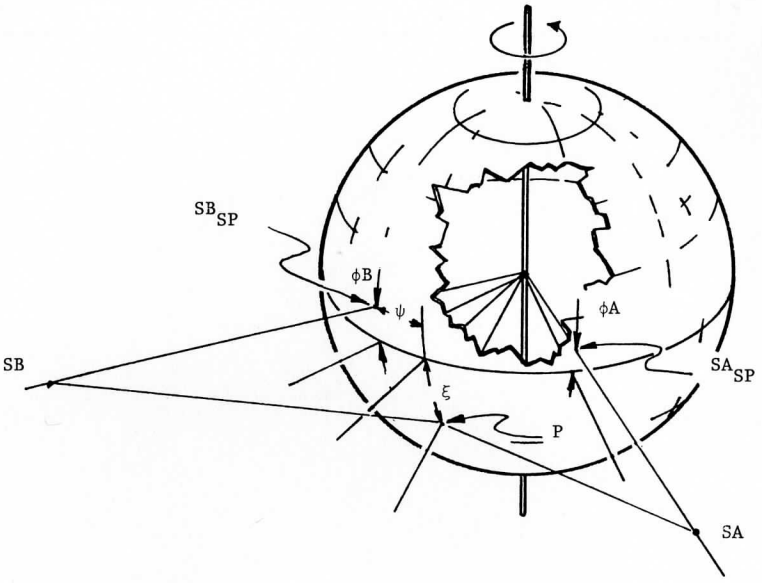

Figure 1. Geometry of the Two Satellite Mapping Problem.

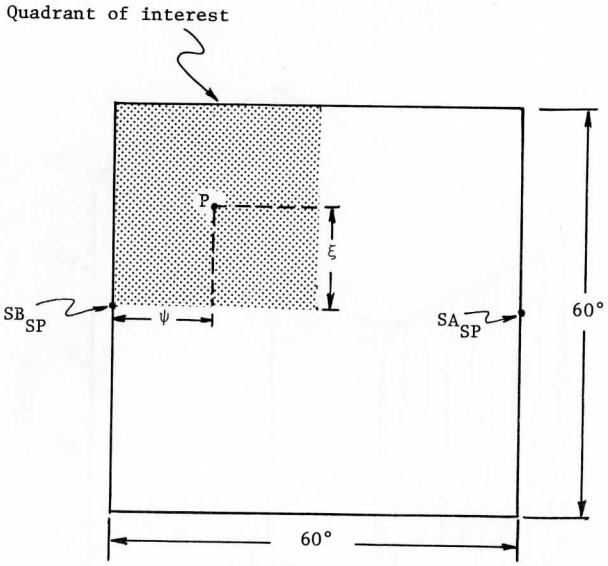

Figure 2. Projection of the Two Satellite Viewing Area on the Earth's Surface.

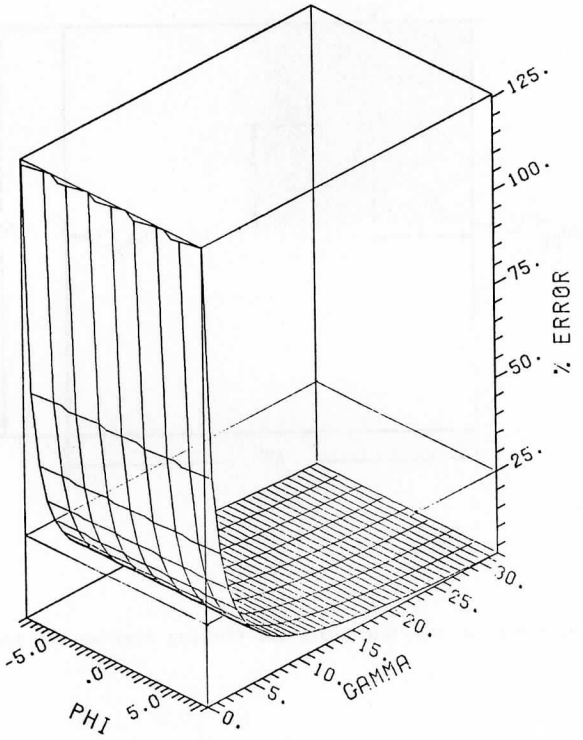

Figure 3. Plot of Normalized Cloud Height Error vs. ψ and γ.

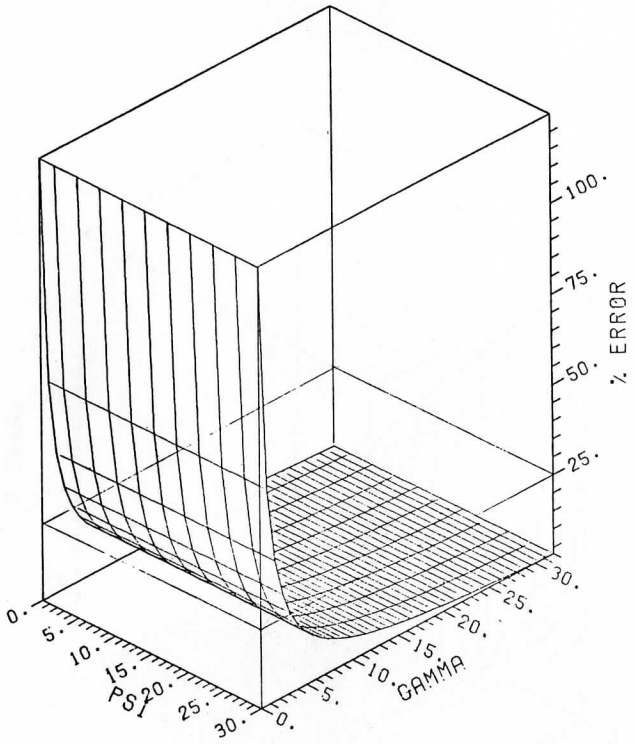

Figure 4. Plot of Normalized Cloud Height Error vs. ϕ and γ.

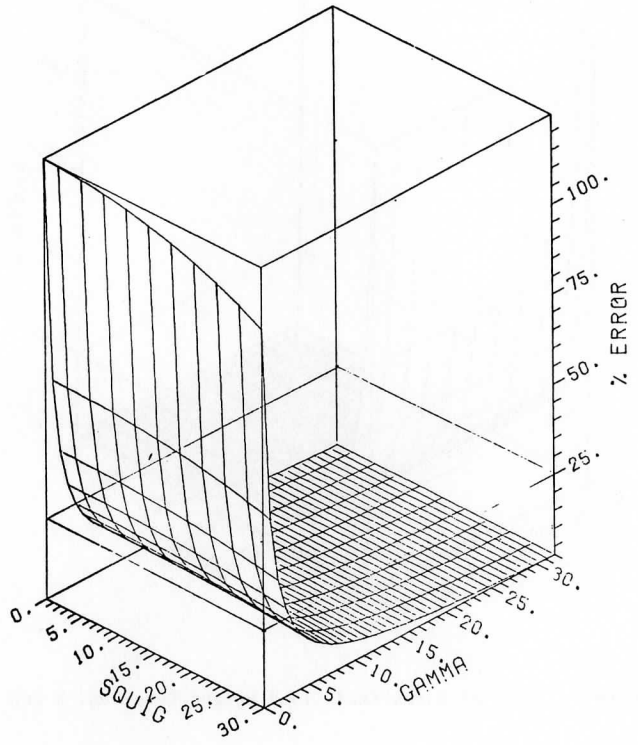

Figure 5. Plot of Normalized Cloud Height Error vs. ξ and γ.

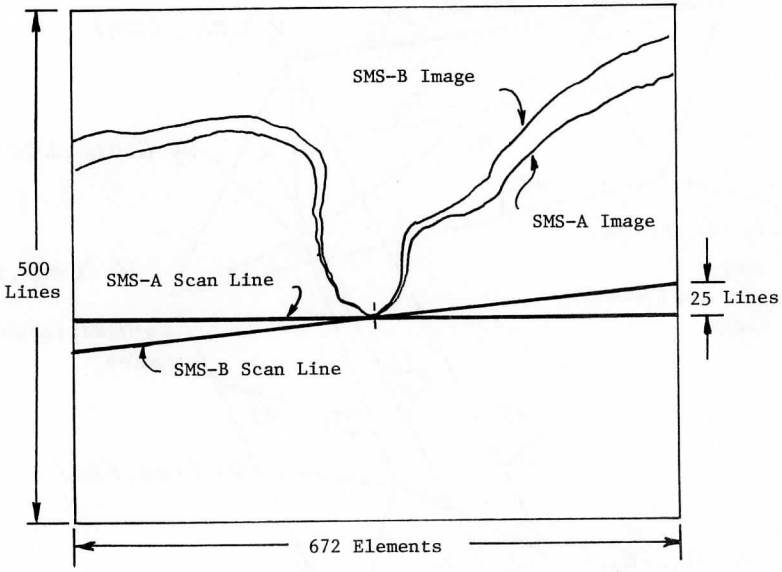

Figure 6. Offset of Scan Line Due to Non-Parallel Spin Axes.

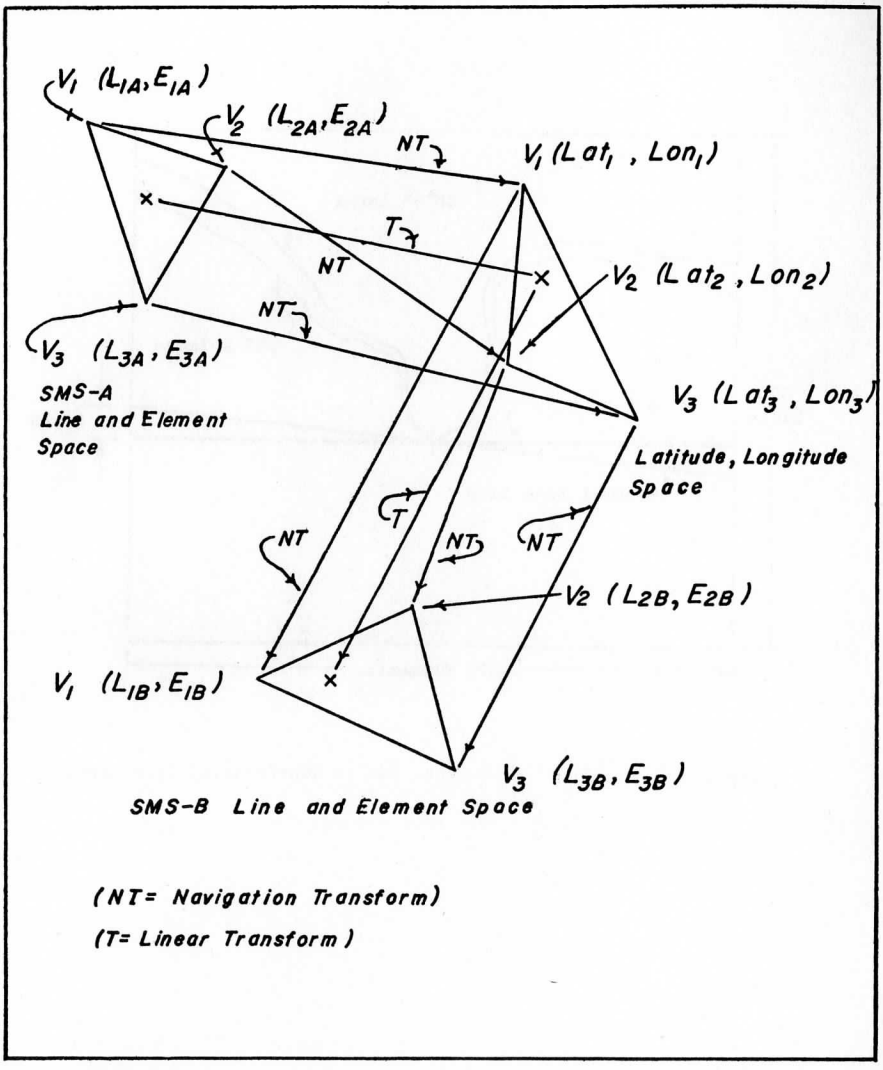

Figure 7. Geometry of the Remapping Problem.

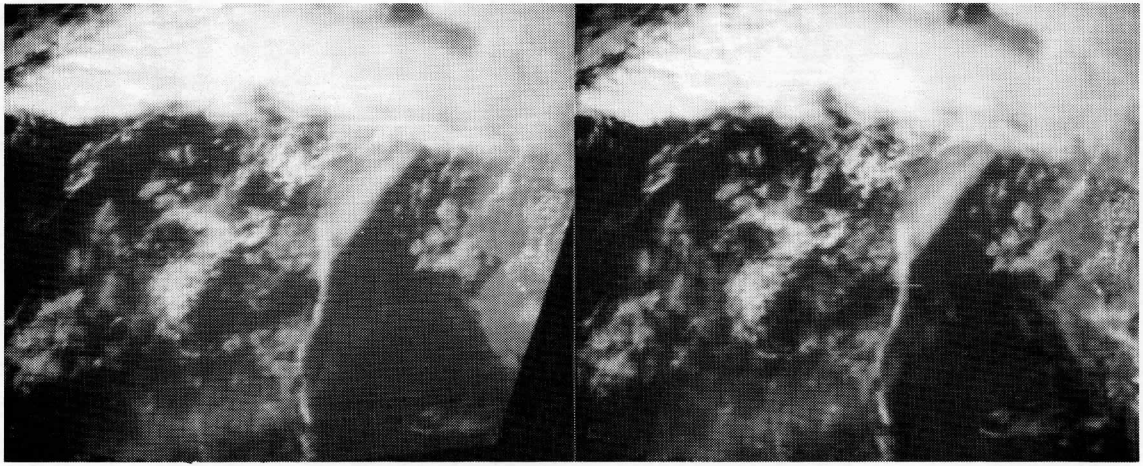

Figure 8. Stereo pair showing the SE Florida coast.

Models for the Determination of Soil and Plant Moisture Parameters Using Remotely Sensed Surface Temperature Data

by

George Diak

ABSTRACT

A simplified ground temperature model is developed for use on the SSEC's interactive computer and video display facility or other sources of appropriate measurements for remote sensing of soil moisture of non-vegetated surfaces. An existing model of leaf temperature is improved to examine the feasibility of sensing moisture in the presence of vegetation. The model will also be useful for heat budget and evapo-transpiration studies.

1. Introduction

Several authors have used different schemes to remotely sense moisture in bare soil. Diak (1975) used the fall of temperature with time at night, and a simplified heat budget condition, to evaluate moisture. Idso et. al. (1975) used a comparison of diurnal temperature range to do the same. Both method have limitations. In the first case simplified observation conditions are required which are sometimes hard to come by. Additionally, the daytime signal which may be beneficial, is not used. In the method of Idso et. al. mentioned above, the detailed characteristics of the individual day, forcing, and response, are not taken into account, reducing the reliability of a single observation. A model taking into account energy forcing and responses could greatly improve a moisture evaluation.

Several authors have studied ground temperature models for remote-sensing and boundary-layer purposes (Sasamori (1970), Rosema (1972)), but these have not been directly coupled with remote-sensing capabilities for a working observation system. The model we use is simplified to reduce computation time and instabilities and make the model interactive with suitable data sources.

Moisture in the soil regulates the soil thermal regime in two ways, through evaporation at the air-soil interface and also due to the changes it causes in the soil's density, heat capacity, and conductivity.

Evaporation in the daytime has the potential to dominate the change in surface temperature. At night, when the latent heat flux may approach zero, thermal conduction may be the dominant process. The difference in the thermal properties (wet to dry), however, produces a surface temperature "signal" which is smaller than the diurnal change due to variation in moisture flux under the same wet to dry conditions. Nebraska data (Lettau 1957) bears out this relationship.

Our new method, incorporating the model, is able to tap this signal caused by evaporation, as well as the nighttime data to improve the signal-to-noise ratio of the system. In future work, several methods may be investigated in an attempt to give the model some vertical resolution. "Pulses" of energy due to a passing cloud, when coupled to a cloud model, may be used in theory as a probe of the vertical structure of soil moisture, since these pulses propagate independently to a depth proportional to the square root of their period. Idso et. al. (1974) have shown that changes in surface albedo are strong indicators of surface moisture changes. Changing albedo might therefore be employed to separate surface water information from that at greater depth.

The below-ground portion of the model is entirely based on conductive energy transfer since water transport for a twenty-four hour observation period is small enough to be neglected as a first approximation.

2. The Physical Model

The transfers of sensible and latent heat in the atmospheric surface layer are computed using the similarity theory of Monin and Obukov (1954), assuming that variations with height of heat, momentum, and water vapor are functions of the non-dimensional height (H/L), where L is the Obukov stability length. (All symbols are defined in table 1).

These profiles are not valid in the layer H less than H_o where H_o is the "roughness height" of the surface. Here the equivalences of fluxes above and below H_o are used to connect the surface layer, to the ground layer. See fig 7.

At the surface the energy balance equation

$$SW\downarrow(1-A) + LW\downarrow + LW\uparrow + SENSIBLE + LATENT + CONDUCTION = 0 \qquad (1)$$

is differentiated with respect to time using the relationship for the fluxes which depend on surface temperature (longwave, sensible, latent) that,

$$\frac{\partial Flux}{\partial t} = \frac{\partial Flux}{\partial T}\,\frac{\partial T}{\partial t} \qquad (2)$$

This time defferential is a means to couple the time rate of change of observed surface temperature into the modeling scheme.

At all levels below the surface the Fourier heat equation (3) is applied.

$$\rho c(\partial T/\partial t) = \partial/\partial Z(K\ \partial T/\partial Z) \qquad (3)$$

The bottom boundary condition is a constant temperature at the lowest subsoil level.

The modeling procedure is a constant spacing, fully implicit, forward-backward procedure of the Crank-Nicolson variety. A grid is laid over the Z, t plane as shown in Fig. 1. A ten-minute time step interval was chosen on the basis of Sasamori's (1975) experiments evaluating his boundary-layer model

time steps. However, the effects of varying time steps can be studied. At each time step the equations are solved using Newton's method.

3. Applications

What is required is a measured infrared surface temperature from the satellite and the hourly standard measurements of wind velocity, air temperature, and relative humidity from Service A. The infrared measurements supply the time-dependent upper boundary condition which the correct solution must match. This can be inferred from equations (1) and (2). Air temperature, humidity, and surface wind speed are needed to parameterize the various flux terms at the surface. Additionally, humidity can be used to refine the standard correction for atmospheric IR emission in the 11.5 μm window due to water vapor (and CO_2) along the path. Visual satellite images are also helpful in determining data quality, especially the presence or absence of small clouds. In data archived at SSEC we have found that clear areas on the order of 100 mi by 100 mi over the required time interval are relatively rare. This means that one must work with 'meso-scale' data. NESS researchers (Smith, 1978) have found that the yeild of high quality satellite soundings can be greatly increased in the presence of clouds by using an interactive system for selecting cloud-free data.

We have come to a similar conclusion; an interactive system for data selection is, at present, a prerequisite for successful use of IR data. At SSEC, McIDAS (Hilyard (ed.), 1977) gives us real-time capability in the infrared to assess surface temperature and to provide complimentary visual imagery. It also has the capability for ingesting and displaying the service A meteorological data which are necessary for the evaluation of heat budget constituents. These characteristics make it very adaptable to the moisture model developed. From this data we can generate, with an initial guess at soil moisture, a curve of surface temperature versus time which can be adjusted and matched at intervals to the real developing situation by varying model moisture content. The best match is then the 'measured' moisture.

Figure 2 displays the flow-chart, including interaction with the McIDAS system.

4. Vegetated Surfaces

The energy relations for a vegetated surface are much more complex than those of bare soil. There are a large variety of vegetation types to contend with, as well as highly varying types of structures within a 'homogeneous' plant canopy.

Data from Ritchie (1974) and Denmead and Shaw (1962) demonstrates that while plants do respond continuously to continuous changes in moisture, there are critical values in moisture where a small difference can make a large difference in plant response (see Fig. 3). It is immediately evident that if the temperature difference of the plants is detectable across this critical change in moisture, there is at least a means to remotely detect stress or no stress conditions via plant temperature.

What magnitude signal can be expected, then, between stress and no-stress conditions? In addition to water stress, the temperature of a plant leaf is influenced by energy relations caused by net radiation, wind speed, humidity, and leaf shape, as well as physiological factors controlling stomatal opening and closing.

Gates (1971) developed a model for estimating the temperature of a leaf with ambient radiation conditions, wind speed, humidity, and leaf dimensions and stomatal resistance as designated parameters. While it was beyond the immediate scope of this work to test his values for transfer coefficients, we felt a more realistic signal amplitude estimate could be achieved with a set of improvements on his basic model. Thus, the model developed differs from his in several important respects.

The Gates model was for a single-surfaced leaf denoting radiant energy input in terms of an 'absorbed power,' a parameter ill-defined for practical purposes.

We sought to define this absorbed power in terms of parameters that meteorologists can measure or approximate such as solar input, albedo, and atmospheric longwave emission to the ground. We added a distinct bottom surface to the leaf and applied an extinction function to the incoming solar radiation through the depth of the leaf layer. Visible and near-infrared radiation were given separate albedo and extinction functions to duplicate characteristics of real leaves. These steps were in recognition of the fact that although energy inputs and outputs averaged over the entire leaf must balance at equilibrium, where energy is applied may make a difference. Radiation conditions seen by the top and bottom are quite different, and this is reflected in the temperature of a leaf's top surface, the one we see with a remote sensor; that is, there is a temperature gradient through the thickness of a leaf. Longwave radiation was applied at the leaf surface since radiation of this wavelength is absorbed very rapidly. Figure 4 shows both the energy balance of our leaf and a flow chart of the model.

Table 2 shows a sample calculation for top and bottom leaf temperatures varying the stomatal resistance. All other parameters are kept constant and are given in the table. As shown, a sizable difference in temperature is predicted as a result of this change in resistance, presumably due to water stress.

Satellite data from day 224, 1977 (Figs. 5a through 5g) shows regions of large horizontal temperature differences over Iowa. Portions of this state were still suffering from drought in late summer 1977.

5. Conclusions

The simplified ground surface model is ready for tuning and testing against real data sources such as the GOES data illustrated in Figs. 5a through 5g. With minor adaptations, the model will be used with data from microwave moisture systems to increase their accuracy, as well as the Heat Capacity Mapping Mission. Price (1977) emphasizes the importance of the heat transfer from soil to atmosphere for an accurate estimate of thermal

inertia. This model is geared to just such an evaluation.

Data gathering for the moisture model emphasizes the important role of an interactive processing system since required evaluations (looking for small cloud 'polluters') of data quality are beyond the capability of current automated techniques, but necessary when IR data are used.

The leaf temperature model is similarly ready for comparison with real data sources and this model may have several uses. Idso et. al. (1972) have recently demonstrated the relationship between remotely sensed canopy temperature and crop yield. For agricultural purposes, it may be beneficial to bypass a direct moisture evaluation and let the plants themselves be indicators of their own status. The model, as outlined in previous section, may be extremely useful for studies of evapotranspiration and heat budget investigations.

ACKNOWLEDGEMENTS

This research has been supported under NASA contract NAS5-24136.

REFERENCES

Aston, A. R. and C. M. M. van Bavel, 1972: Soil Surface Water Depletion and Leaf Temperature. Agricultural Journal, 64, 368-373.

Bussinger, J. A., 1973: Turbulent Transfer in Atmospheric Surface Layer, Workshop on Micrometeorology. D. Haugen (ed), Boston, Am. Meteor. Soc.

Denmead, O. T. and R. H. Shaw, 1962: Availability of Soil Water to Plants as Affected by Soil, Moisture Content and Meteorological Conditions. Agricultural Journal, 54, 390-395.

Diak, G. R., 1977: A Radiative Transfer Scheme of Soil Moisture Remote Sensing, Studies of Soundings and Imaging Measurements. Final report on NAS5-21798, Madison, Wisconsin, July, pp. 65-79.

Gates, D. M. and L. Papian, 1971: Atlas of the Energy Budget of Plant Leaves. Academic Press, New York.

Herman, G. F., 1975: Radiative-Diffusive Models in the Arctic Boundary Layer, Scientific Rept. No. 3, Massachusetts Institute of Technology Dept. Meteor., July 25.

Hilyard, Joseph (ed.), 1977: Interactive Video Desplays for Atmospheric Studies, Proceedings of a workshop at the University of Wisconsin-Madison, 14-16 June 1977.

Idso, S. B., R. D. Jackson and R. J. Reginato, 1977: Remote Sensing of Crop Yields. Science.

_____, 1975: Detection of Soil Moisture by Remote Surveillance. American Scientist, Sept - Oct, pp. 549-556.

Idso, S. B., R. D. Jackson, R. J. Reginato, B. A. Kimball and F. S. Nakayama, 1975: The Dependence of Bare Soil Albedo on Soil Water Content. J. Appl. Meteor., 14, 109-113.

Idso, S. B., T. J. Schmugge, R. D. Jackson and R. J. Reginato, 1975: The Utility of Surface Measurements for the Remote Sensing of Surface Soil and Water Status. J. Geophys. Res., 80, 3044-3049.

Letteau, H. H. and B. Davidson, 1957: Exploring the Atmosphere's First Mile. Vol. II, New York, Pergamon Press.

Monin A. S. and A. M. Obukov, 1954: Basic Regularity in Turbulent Mixing in the Surface Layer of the Atmosphere. USSR Academy of Science Geophysical Institute, No. 24.

Monteith, J. L., 1971: Ecology by Computer. Nature. 231, 540.

Nahashabandi, A. and H. Kohnke, 1965: Thermal Conductivity and Diffisivity of Soils as Related to Moisture Tension and other Physical Properties. Agricultural Meteorology, 2, 271-279.

Paulson, C. A., 1970: The Mathematical Representation of Wind Speed and Temperature Profiles in the Unstable Atmospheric Surface Layer. J. Appl. Meteor., 9, 857-861.

Ritchie, J. T., 1973: Influence of Soil Water Status and Meteorological Conditions on Evaporation from a Corn Canopy. Agricultural Journal, 65, 893-897.

Rasema, A., 1975: Simulation of the Thermal Behavior of Bare Soils for Remote Sensory Purposes. Advances in Thermal Engineering, Vol. 3, Heat and Mass Transfer in the Biosphere. DeVries & Afgan (ed), John Wiley and Sons, New York.

Sasamori, T., 1970: A Numerical Study of Atmosphere and Soil Boundary Layers. J. Appl. Meteor., 27, 1122-1137.

Table 1. List of Symbols

A	Albedo (dimension less)
C	Specific heat (Joules $kg^{-1} \cdot deg^{-1}$)
H	Height above surface (m)
H_o	Roughness height (m)
h	Model soil depth increment (m)
K	Soil thermal conductivity (Watts$\cdot m^{-1} \cdot deg^{-1}$)
k	Model time increment (s)
LW↓	Downwelling longwave radiation (Watts$\cdot m^{-2}$)
LW↑	Upwelling longwave radiation (Watts$\cdot m^{-2}$)
SW↓	Incident shortwave radiation (Watts$\cdot m^{-2}$)
T	Temperature (K)
h	Subsoil depth increment (m)
k	Model time increment (s)
t	Time (s)
Z	Depth below surface (m)
ρ	Soil density ($kg \cdot m^{-3}$)

Table 2. Variation of leaf temperature with stomatal resistance

The following conditions apply: Wind speed at canopy level 0.5 m s^{-1}; total visible and near IR radiation 1115 watts m^{-2} (equivalent to 1.6 cal cm^{-2} min^{-1}); leaf size 0.2 m by 0.1 m; air temperature 300K; relative humidity 50 percent.

Stomatal Resistance (sec cm^{-1})*	0	2	5	10	30
Leaf Temperature					
upper surface	296.7	302.1	304.7	306.2	307.6
lower surface	291.7	295.3	297.0	298.0	298.9

*Multiply by 100 to convert to Sec m^{-1}

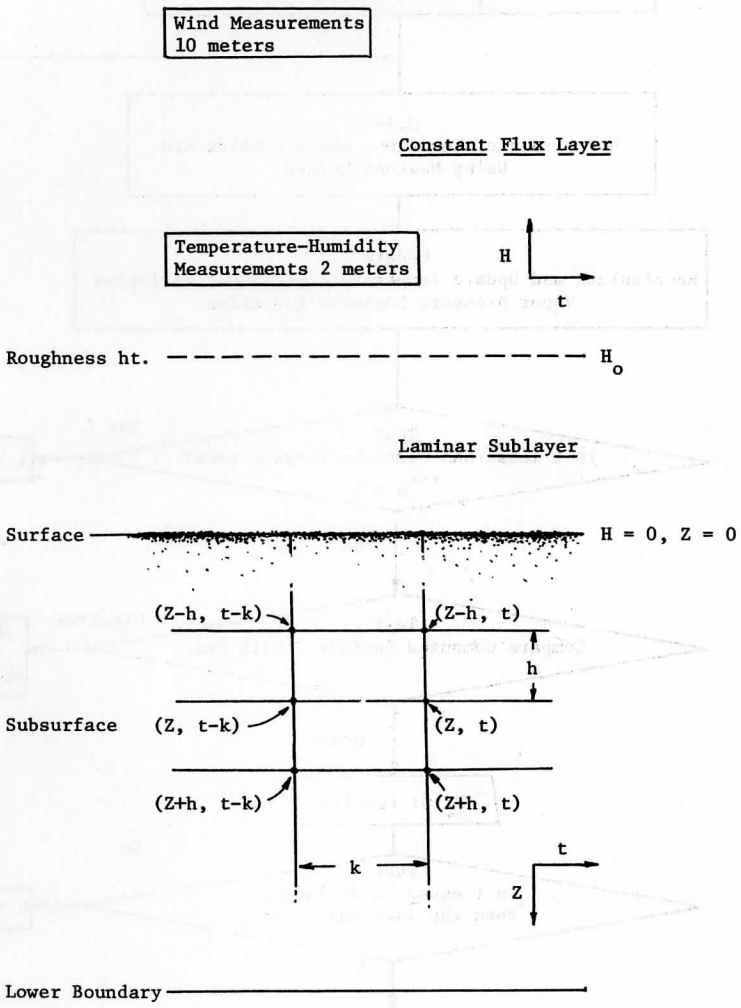

Fig. 1 Schematic Computational Space-Time Grid

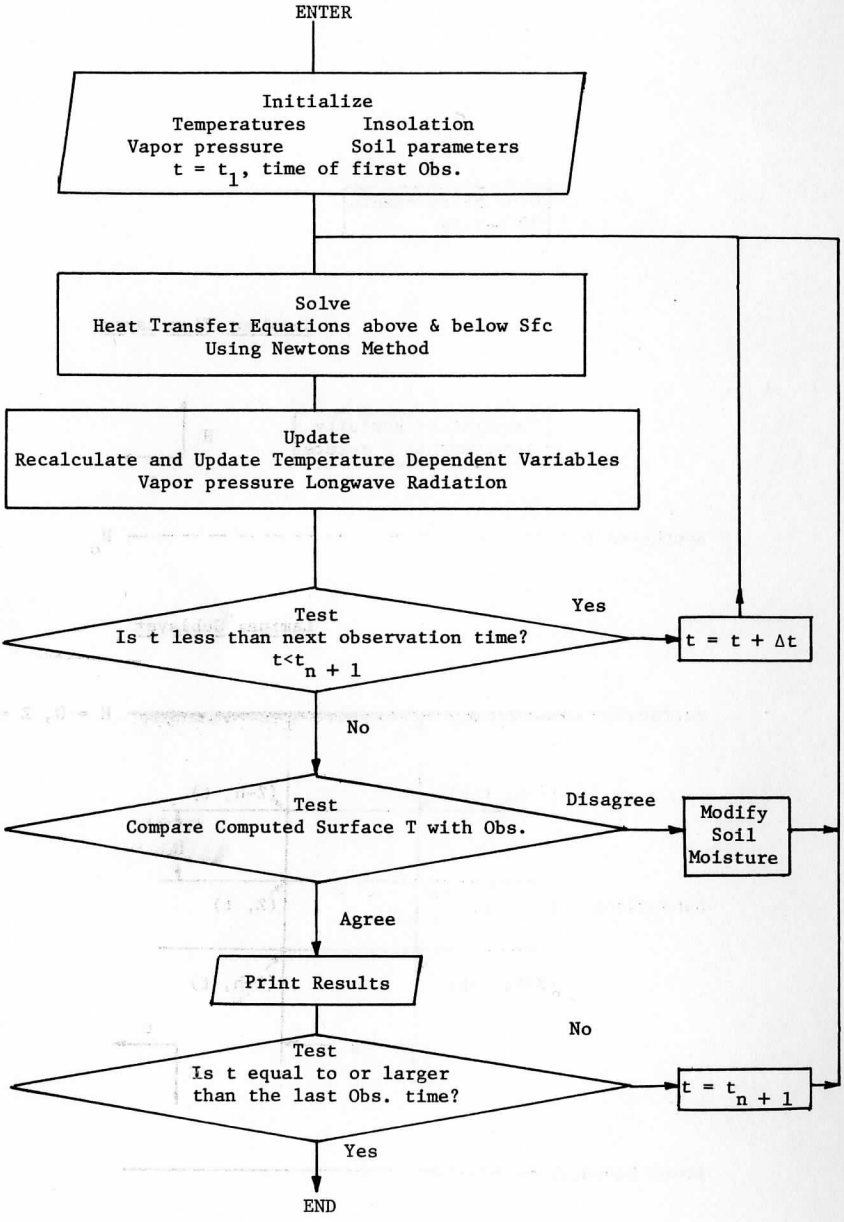

Fig. 2 Flow Chart of Soil-Temperature Model

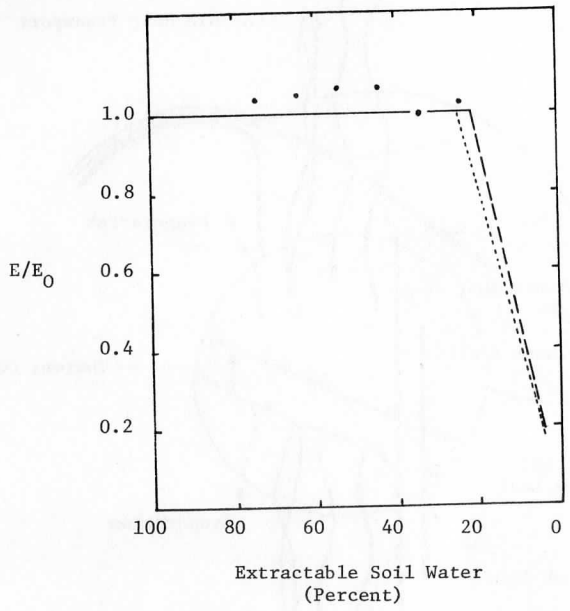

Fig. 3 Ratio of Evapotranspiration to Potential

Evapotranspiration as a Function of Soil Moisture for Four Crops. The figure was redrawn from Aston and van Bavel (1972). The points represent corn, the dashed curve alfalfa, and the dotted curve cotton and sorghum. Note that the plotted values for corn excede the theoretically derived maximum value 1.0. Aston and van Bavel attribute this to an error in the calculation of potential evapotranspiration. The significant feature of this graph is the 'sudden onset' of stress, as evidenced by a sharp change of E/E_o near 20 percent extractable water. This sharp change is produced by an increase in stomatal resistance.

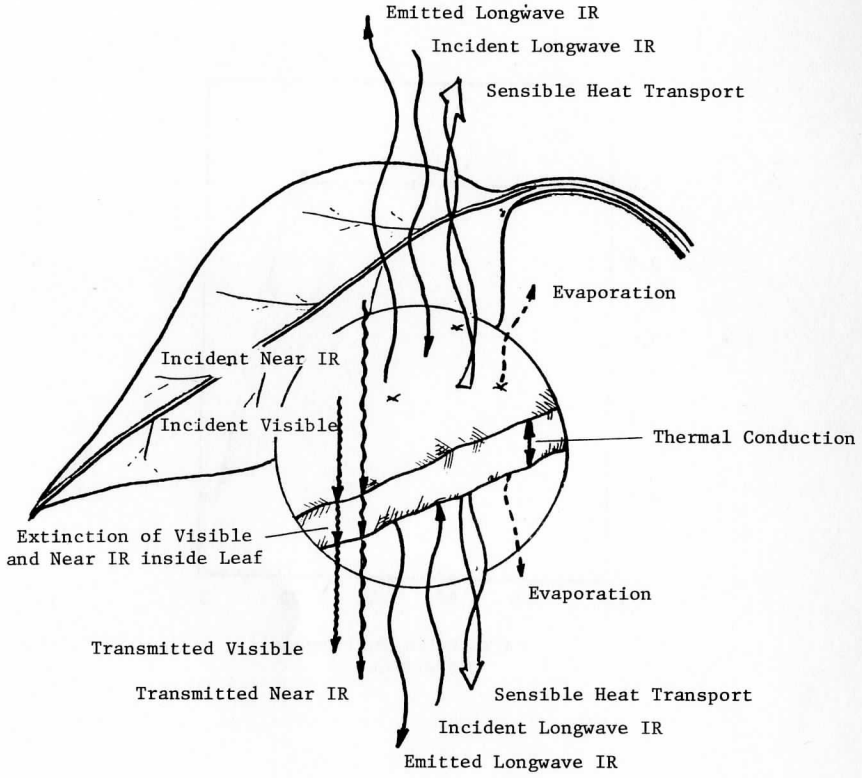

Figure 4a

Fig. 4 Leaf Energy Balance, Calculation of Leaf Temperature and Determination of Plant Moisture Status. As the soil moisture approaches the 'knee' region of Fig. 3 evaporation drops sharply, thus the leaf temperature rises, increasing both sensible heat transport and longwave emission, to restore energy balance. Detailed calculation of the balance results in an estimate of plant moisture status as shown in the flow chart.

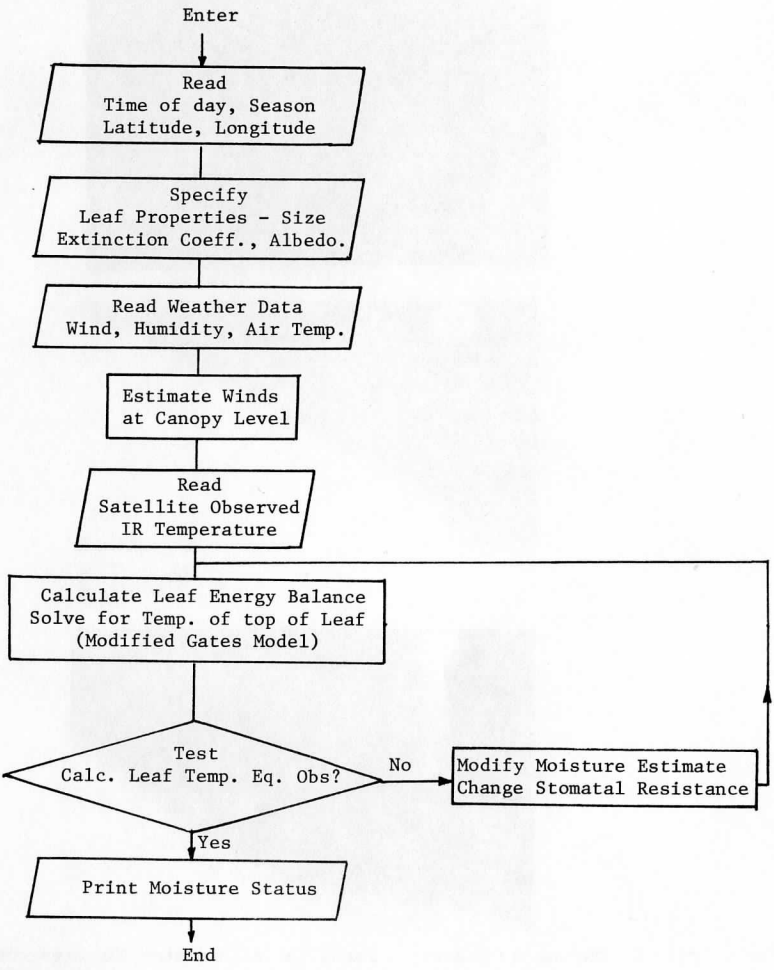
Enter
Read
Time of day, Season
Latitude, Longitude
Specify
Leaf Properties - Size
Extinction Coeff., Albedo.
Read Weather Data
Wind, Humidity, Air Temp.
Estimate Winds
at Canopy Level
Read
Satellite Observed
IR Temperature
Calculate Leaf Energy Balance
Solve for Temp. of top of Leaf
(Modified Gates Model)
Test
Calc. Leaf Temp. Eq. Obs?
No
Modify Moisture Estimate
Change Stomatal Resistance
Yes
Print Moisture Status
End

Figure 4b

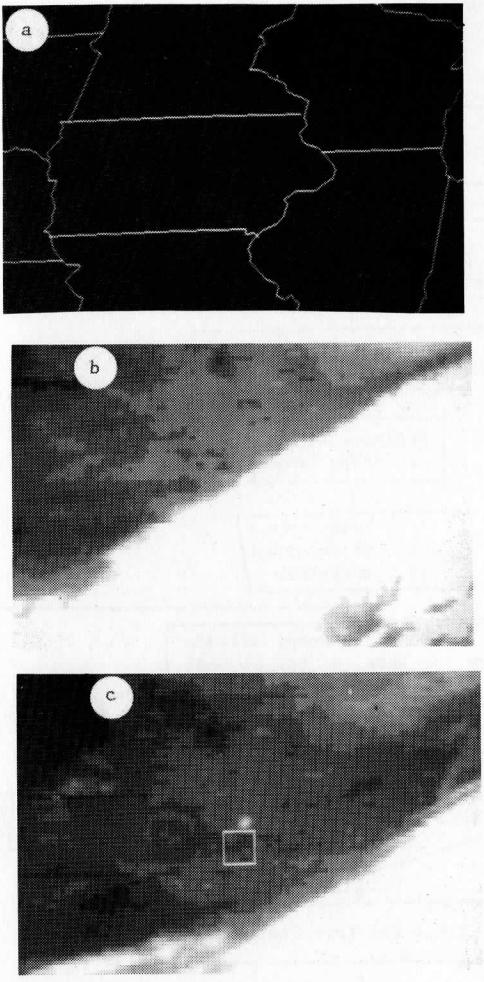

Fig. 5 Thermal IR History. Panel (a) illustrates the area covered by the remaining parts of the figure. Panel (b) shows 1800 UT on day 223 of 1977, (c) shows 2200 UT the same day, while (d) is 0200 UT of day 224 and (e) is 0800 UT of day 224. The temperature difference from 2200 to 0800 UT is shown in (f) and the 0200 to 0800 UT temperature difference in (g). For (b) through (e) lighter shades are relatively cool, darker shades relatively warm. In (f) and (g) dark shades imply a small temperature drop, light shades, a larger temperature fall. Salient features are: The relatively large pixel size; the constant temperature of larger bodies of water (Green Bay, Lake Michigan) and the prominance of the Mississippi Valley; the existence of well defined thermal features on a scale of $\approx$10 pixels; discernable effects of clouds at the upper and lower edges of some of the pictures; and the changing patterns in (b) through (e).

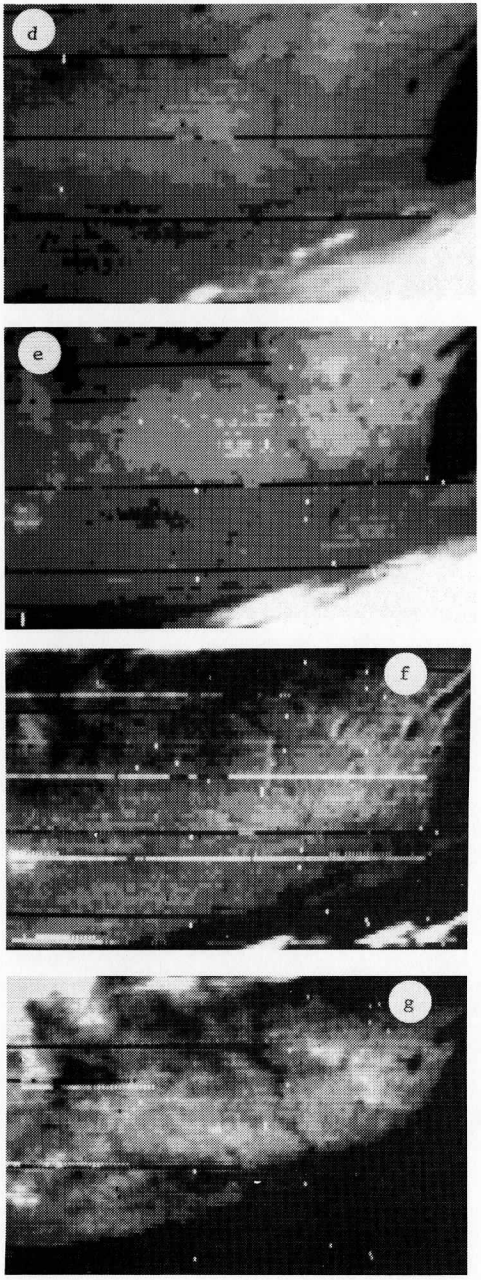

Figure 5

REPORTS AVAILABLE FROM

THE UNIVERSITY OF WISCONSIN PRESS, BOX 1379, MADISON, WISCONSIN 53701

97024. Studies in Atmospheric Energetics Based on Aerospace Probings: Annual Report, 1966. 129 pages. 1967. $5.00

97026. Studies in Atmospheric Energetics Based on Aerospace Probings: Annual Report, 1968. 162 pages. 1969. $5.00

97027. Radiation Experiment in the Vicinity of Barbados: Final Report, NSF Grant Ga. 12603. 100 pages. 1970. $5.00

97028. The Study of Radiation in a Tropical Atmosphere: Final Report. 100 pages. 1970. $5.00

97029. The Educational and Social Uses of Communications Satellites: A Bibliography. 42 pages. 1970. $3.50

97030. Measurements from Satellite Platforms; Annual Scientific Report on NAS5-11542, 1968-69. 388 pages. 1970. $10.00

97031. A Pilot Study on the Application of Geosynchronous Meteorological Satellite Data to Very Short Range Terminal Forecasting. 113 pages. 1970. $5.00

97032. Studies of the Atmosphere Using Aerospace Probings: Annual Report, 1969. 243 pages. 1970. $7.50

97033. Teleconferencing: A Bibliography. 42 pages. 1971. $3.50

97034. Legal and Political Aspects of Satellite Telecommunication: An Annotated Bibliography. 126 pages. 1971. $7.50

97035. Multidisciplinary Studies of the Social, Economic and Political Impact Resulting from Recent Advances in Satellite Meteorology: An Interim Report, Vol. 1. 459 pages. 1971. $7.50

97036. Multidisciplinary Studies of the Social, Economic and Political Impact Resulting from Recent Advances in Satellite Meteorology: An Interim Report, Vol. 2. 431 pages. 1971. $15.00

97037. Measurements from Satellite Platforms: Annual Scientific Report on NAS5-11542, 1969-70. 180 pages. 1971. $7.50

97038. Studies of the Atmosphere Using Aerospace Probings: Annual Report, 1970. 69 pages. 1971. $5.00

97039. Legal Aspects of Satellite Teleconferencing. 213 pages. 1971. $7.50.

97040. Teleconferencing in Wisconsin. 240 pages. 1971. $10.00

97041. Measurements from Satellite Platforms: Annual Scientific Report on NAS5-11542, 1970-71. 270 pages. 1972. $10.00

97042. Experiments in Medical Communications via the ATS-1 Satellite. 136 pages. 1972. $7.50

(continued from back cover)

97043. Specifications for a Vertical Temperature and Moisture Sounder for the Synchronous Meteorological Satellites. 82 pages. 1972. $5.00

97044. Scientific Requirements of Sea Surface Measurements for the GARP Tropical Experiment. 18 pages. 1972. $2.50

97045. Studies of the Atmosphere Using Aerospace Probings: Annual Report, 1971, Vol. II: Application Studies. 104 pages. 1972. $5.00

97046. Multidisciplinary Studies of the Social, Economic and Political Impact Resulting from Recent Advances in Satellite Meteorology: An Interim Report, Vol. 3. 252 pages. 1972. $10.00

97047. Multidisciplinary Studies of the Social, Economic and Political Impact Resulting from Recent Advances in Satellite Meteorology: An Interim Report, Vol. 4. 199 pages. 1972. $10.00

97048. Satellite Teleconferencing: An Annotated Bibliography. 130 pages. 1972. $7.50

97049. Measurements from Satellite Platforms: Annual Scientific Report on NAS5-11542, 1971-72. 228 pages. 1972. $7.50

97050. Synchronous Meteorological Satellite Sounder Specification: Final Report under NASA Contract NAS5-21607. 73 pages. $5.00rr

97051. Multidisciplinary Studies of the Social, Economic and Political Impact Resulting from Recent Advances in Satellite Meteorology: An Interim Report, Vol. 5. 290 pages. 1973. $10.00

97052. Measurements from Satellite Platforms: Annual Scientific Report on NAS5-21798, 1972-73. 331 pages. 1974. $10.00

97053. Visual Channel Data Analysis for Synchronous Meteorological Satellite: Scientific Report on NOAA/NESS Grant NG-26-72. 252 pages. 1974. $7.50

97054. Studies of the Atmosphere Using Aerospace Probes. Annual Report, 1973. 272 pages. 1974. $7.50

97055. Meteorological Measurements from Satellite Platforms: Annual Scientific Report on NAS5-21798, 1973-74. 97 pages. 1975. $5.00

97056. Studies of the Atmosphere Using Aerospace Probes. Annual Report, 1974. 154 pages. 1975. $5.00

97057. Multidisciplinary Studies of the Social, Economic and Political Impact Resulting from Recent Advances in Satellite Meteorology: Final Report, Vol. 6. 100 pages. $10.00

97058. Studies of the Atmosphere Using Aerospace Probes. Annual Report, 1975. 91 pages. $7.50

97059. Studies of Soundings and Imaging Measurements. Final Scientific Report on NAS5-21798, 1974-1976. 273 pages. 1977. $10.00

97060. Studies of the Atmosphere Using Aerospace Probes. Annual Report, 1976. 238 pages. 1977. $7.50